Five Low-Noise Stable Oscillators Referenced to the Same Multimode AlN/Si MEMS Resonator

Tahmid Kaisar, *Graduate Student Member, IEEE*, S M Enamul Hoque Yousuf, *Graduate Student Member, IEEE*, Jaesung Lee, *Member, IEEE*, Afzaal Qamar, *Member, IEEE*, Mina Rais-Zadeh, *Senior Member, IEEE*, Soumyajit Mandal, *Senior Member, IEEE*, and Philip X.-L. Feng, *Senior Member, IEEE*

***Abstract*—We report on the first experimental demonstration of five self-sustaining feedback oscillators referenced to a single multimode resonator, using piezoelectric aluminum nitride on silicon (AlN/Si) microelectromechanical systems (MEMS) technology. Integrated piezoelectric transduction enables efficient readout of five resonance modes of the same AlN/Si MEMS resonator, at 10, 30, 65, 95, and 233 MHz with quality (*Q*) factors of 18 600, 4350, 4230, 2630, and 2138, respectively, at room temperature. Five stable self-sustaining oscillators are built, each referenced to one of these high-*Q* modes, and their mode-dependent phase noise and frequency stability (Allan deviation) are measured and analyzed. The 10, 30, 65, 95, and 233 MHz oscillators exhibit low phase noise of −116, −100, −105, −106, and −92 dBc/Hz at 1 kHz offset frequency, respectively. The 65 MHz oscillator yields the Allan deviation of 4×10^{-9} and 2×10^{-7} at 1 and 1000 s averaging time, respectively. The 10 MHz oscillator's low phase noise holds strong promise for clock and timing applications. The five oscillators' overall promising performance suggests suitability for multimode resonant sensing and real-time frequency tracking. This work also elucidates mode dependency in oscillator noise and stability, one of the key attributes of mode-engineerable resonators.**

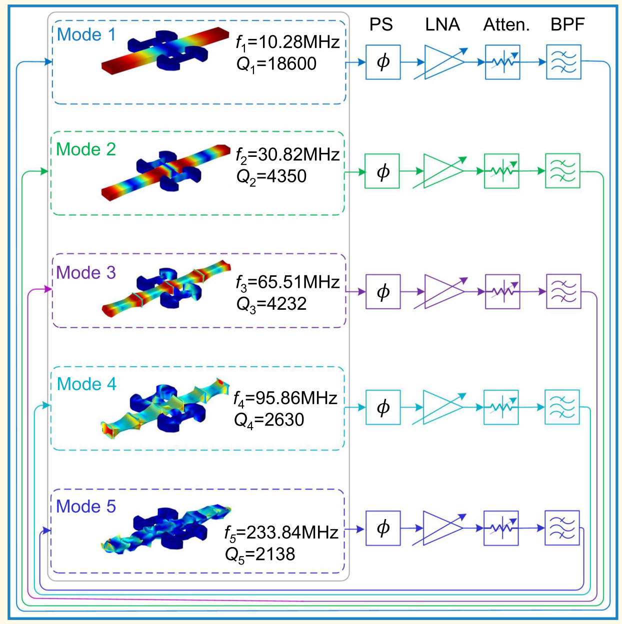

***Index Terms*—Allan deviation, microelectromechanical systems (MEMS), multimode resonator, phase noise, piezoelectric aluminum nitride on silicon (AlN/Si), self-sustaining feedback oscillators.**

I. Introduction

OVER the past two decades, radio frequency (RF) microelectromechanical system (MEMS) resonators have attracted great attention in a variety of research fields [1], [2], [3], [4], [5], [6]. For next-generation wireless communication, there is a rising need for high-performance, single-chip, multiband, and customizable RF solutions. A stable frequency source is essential for RF transceivers since it serves as a reference signal for signal modulation and synchronization. A reconfigurable multifrequency source is desirable when a single-chip multiband RF solution is required [7]. Usually, phase-locked loop (PLL) frequency synthesizers are used as programmable frequency sources in RF transceivers [8]. However, the addition of a PLL greatly enhances the system's overall power consumption and the chip area devoted to the oscillator. Furthermore, the output signal's phase noise is increased by at least $20\log(N)$ dB when the PLL produces a high-frequency signal by multiplying the frequency of a reference oscillator [usually based on quartz or surface acoustic wave (SAW) resonators] by an integer or fractional

Manuscript received 7 February 2023; accepted 19 April 2023. Date of publication 5 September 2023; date of current version 13 October 2023. This work was supported in part by the National Science Foundation (NSF) via the Division of Computing and Communication Foundations (CCF) Foundations of Emerging Technologies (FET) Program under Grant CCF-2103091, in part by the Army Research Office (ARO) under Grant W911NF-16-1-0340, and in part by the Air Force Office of Scientific Research under Grant FA9550-23-1-0304. *(Corresponding author: Philip X.-L. Feng.)*

Tahmid Kaisar, S M Enamul Hoque Yousuf, and Philip X.-L. Feng are with the Department of Electrical and Computer Engineering, Herbert Wertheim College of Engineering, University of Florida, Gainesville, FL 32611 USA (e-mail: kaisart@ufl.edu; syousuf@ufl.edu; philip.feng@ufl.edu).

Jaesung Lee is with the Department of Electrical and Computer Engineering, Herbert Wertheim College of Engineering, University of Florida, Gainesville, FL 32611 USA, and also with the Department of Electrical and Computer Engineering, University of Central Florida, Orlando, FL 32816 USA (e-mail: jaesung.lee@ucf.edu).

Afzaal Qamar is with the Department of Electrical and Computer Engineering, University of Michigan, Ann Arbor, MI 48109 USA (e-mail: afzaalqamar@gmail.com).

Mina Rais-Zadeh is with the Department of Electrical and Computer Engineering, University of Michigan, Ann Arbor, MI 48109 USA, and also with the Jet Propulsion Laboratory, California Institute of Technology, Pasadena, CA 91109 USA (e-mail: mina.rais-zadeh@jpl.nasa.gov).

Soumyajit Mandal is with the Brookhaven National Laboratory, Upton, NY 11973 USA (e-mail: smandal@bnl.gov).

Digital Object Identifier 10.1109/TUFFC.2023.3312159

Highlights

- **Demonstration of five stable self-sustaining feedback oscillators referenced to single multimode AlN/Si MEMS resonator for the first time.**
- **The 10, 30, 65, 95 and 233 MHz oscillators exhibit low phase noise of −116, −100, −105, −106 and −92 dBc/Hz at 1 kHz offset frequency, respectively.**
- **The five oscillators' overall promising performance suggests suitability for multimode resonant sensing and tracking and elucidates mode dependency in oscillator noise and stability.**

value N [8]. Instead of using a PLL, programmable MEMS oscillators can be utilized to produce stable and accurate frequency reference sources for integer-N or fractional-N frequency synthesizers [9]. This strategy is advantageous because it enables the dynamic selection of frequency references for the best performance in each operational area. For application in ultralow-power IoT sensor nodes, for instance, a low-frequency MEMS resonant mode with high Q and strong long-term stability can be chosen due to the requirement for low power, compactness, low cost, and precise frequency references [10], [11]. On the contrary, a high-frequency mode can be utilized for agile frequency synthesis for future reconfigurable RF front ends.

Recently, self-sustaining feedback oscillators using high-QMEMS resonators as their frequency selecting elements have become competitive or even better alternatives to traditional quartz crystal oscillators [12], [13], [14], [15], [16]. Indeed, programmable oscillators referenced to MEMS resonators are now available commercially with impressive specifications for timing applications. Some of the latest MEMS temperature-compensated crystal oscillator (TCXO) products from SiTime using single-crystal Si resonators already achieve long-term stabilities better than ±100 ppb over the commercial temperature range [17].

Due to their miniaturized dimensions, resonant MEMS and nanoelectromechanical systems (NEMS) exhibit very high responsivities to very small force, displacement, and mass variations by converting them into small frequency shifts that can be measured, thus enabling new resonant sensors with unprecedented single-charge, single-molecule, and single-atom sensitivities or resolutions [18], [19], [20], [21], [22], [23], [24], [25], [26].

Over the past decade, mass sensing with NEMS resonators has systematically improved to the point where they now offer impressive capabilities for a new promising approach to mass spectrometry [25], [26], [27], [28]. In proof-of-concept experiments, carbon nanotube NEMS resonators have demonstrated mass detection limit down to the yoctogram (10^{-24} g) level, which is at the single proton mass sensitivity [29].

MEMS and NEMS resonators with multiple modes become attractive as they can enhance the sensing performance and also enable new sensing modalities. For example, while a particle is attached to a cantilever beam, the frequency shift is dependent on the location of the particle with respect to the mode shapes. If a particle lands at the antinodes, large frequency shifts are expected, while if the particle lands at the nodal points, a minimal frequency shift is expected. By using this mode-dependent information, an inertial imaging technique has been proposed in which the NEMS resonators and arrays can not only sense the particles but also can resolve their sizes and spatial distributions [30], [31], [32], [33]. This opens an avenue toward nanomechanical imaging of distributed biological species.

Given the important motivating forces discussed earlier, the objectives of our work have been focused on: 1) studying high-Q multimode resonators and 2) building stable, low-noise multimode oscillators to enable new MEMS clocks for real-time frequency tracking and sensing capabilities. In our previous work, we have demonstrated three stable self-sustaining oscillators referenced to the same multimode aluminum nitride on silicon (AlN/Si) MEMS resonator [34]. Here, we extend the earlier work by demonstrating, for the first time, five stable, low-noise feedback oscillators or clocks at ∼10, 30, 65, 95, and 233 MHz, referenced to the 1st, 2nd, 3rd, 4th, and 5th length extensional (LE) modes, respectively, of a single AlN/Si MEMS resonator. Fig. 1 shows an overview of the concept, schematic design, and key outcome of this work. Existing demonstrations of MEMS oscillators in such frequency ranges have been based on electrostatically transduced 10 MHz beam [35] and ∼60 MHz wine-glass disk resonators [15], 11 MHz double-ended tuning fork (DETF) resonators [36], and ∼10 MHz Ni micromechanical resonators [37]. Although simultaneous dual-mode excitation of bulk acoustic wave (BAW) MEMS resonator-based oscillator has been demonstrated for self-temperature sensing [38], stable self-sustaining oscillators with more than two clock frequencies generated by the same MEMS resonator, and their mode dependency on phase noise and Allan deviation performance, have not yet been reported.

Different modes have different effective masses, quality (Q) factors, and power handling capabilities that set the ultimate limits of phase noise and Allan deviation performance metrics. In light of this fact, it is crucial to investigate the mode dependency of phase noise and frequency stability (Allan deviation) of multimode oscillators in the context of real-time sensing and timing (clock) applications.

In this work, we employ all-piezoelectric transduction built into AlN/Si MEMS to study five modes of the same resonator and build a self-sustaining oscillator for each mode. We observe a phase noise of −116 dBc/Hz at 1 kHz offset for the oscillator of the fundamental mode (10.28 MHz), lower than those in the other modes. Oscillators referenced to the 2nd mode (30.82 MHz), 3rd mode (65.51 MHz), 4th mode (95.86 MHz), and 5th mode (233.84 MHz) also exhibit excellent and promising performance in phase noise and frequency stability. In particular, oscillators referenced to

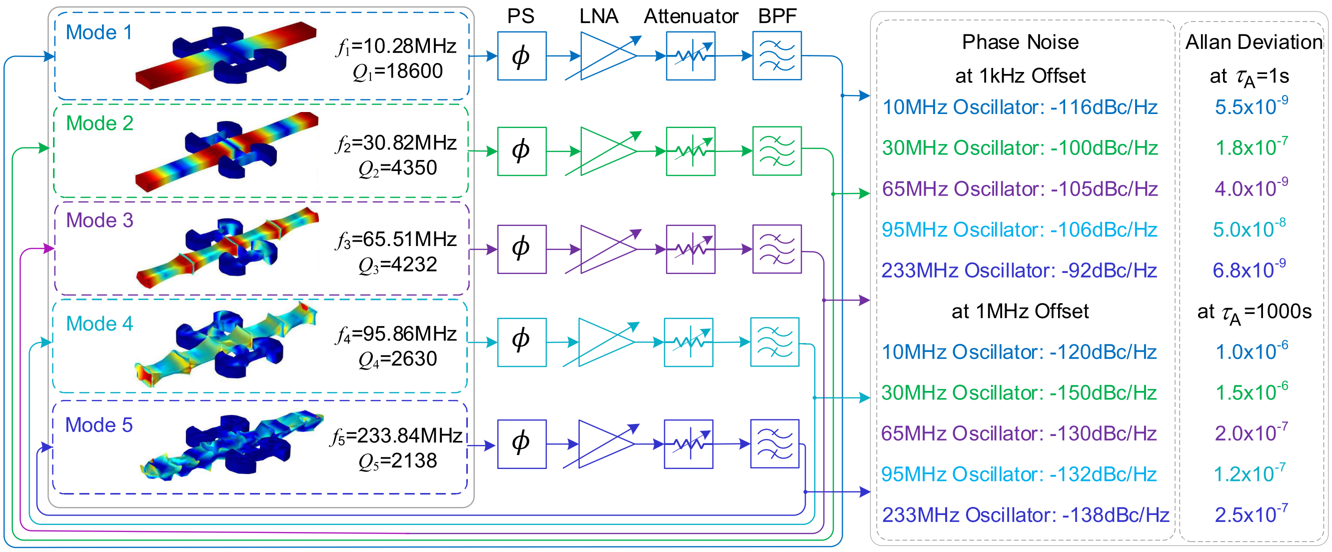

Fig. 1. Schematic illustration of the design and demonstration of five stable self-sustaining oscillators referenced to five high-Q resonance modes of the same piezoelectric AlN/Si MEMS resonator. The panels on the right highlight the excellent performance achieved by the five oscillators, in both phase noise and Allan deviation specifications, all have been measured at room temperature and in moderate vacuum (~20 mTorr) that is readily attainable by state-of-the-art packaging technologies. PS, LNA, and BPF stand for phase shifter, low-noise amplifier, and bandpass filter, respectively.

the 1st mode, 3rd mode, and 5th mode offer state-of-the-art comparable combined short- and long-term Allan deviation specifications.

II. Device Design, Fabrication, and Characterization

The resonance frequency of an LE mode resonator is chosen in such a way so that it is independent of the resonator's thickness. The fundamental LE mode resonance frequency of the resonator can be written as [39]

$$f_0 = \frac{1}{2L}\sqrt{\frac{t_1 E_{Y1} + t_2 E_{Y2}}{t_1\rho_1 + t_2\rho_2}} \tag{1}$$

where t_1, ρ_1, and E_{Y1} are the thickness, mass density, and Young's modulus of Si, respectively, and t_2, ρ_2, and E_{Y2} are the thickness, mass density, and Young's modulus of AlN, respectively. The resonator is designed to have the fundamental LE mode at 10 MHz, so the length is chosen to be 480 μm as found from the finite element method (FEM) simulations using COMSOL Multiphysics.

The AlN/Si MEMS resonator fabrication [40] starts with a double-side polished Si-on-insulator (SOI) wafer with a 20 μm-thick phosphorus-doped (at 4.6 $\times$ 10^{19} cm^{-3} with a resistivity of 1.59 MΩ-cm) Si layer and a 500 μm Si substrate (see Fig. 2). By maintaining the high thickness ratio of the Si substrate to the other layers, the mechanical loss is minimized. A layer of 1 μm AlN (piezoelectric layer) is sputtered on top of the highly doped Si layer and 100 nm Al for metal routing is deposited as the top electrode and patterned through the liftoff process. The reasons for using Al as metal routing are: 1) its good adhesion to AlN and 2) similar acoustic properties to AlN, which reduce losses. Si can act as the ground layer electrode for the piezoelectric stack, reducing the number of layers and minimizing interface loss. Reactive ion etching

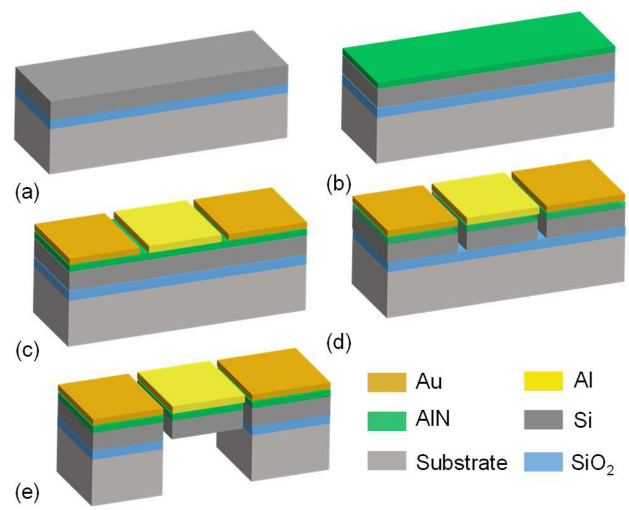

Fig. 2. AlN/Si resonator fabrication process. (a) SOI wafer. (b) AlN deposition. (c) Electrode patterning using liftoff process. (d) RIE to define the resonator dimensions. (e) DRIE to release the device and form free-standing structure.

(RIE) through the buried oxide layer is used to define the dimensions of the resonator. Finally, the device is released from the back side using deep RIE (DRIE) and the buried oxide layer is also removed.

A. Equivalent Circuit Model

We have derived a lumped equivalent circuit model using Cadence Virtuoso for each mode. All modes have motional resistance of less than 2.1 kΩ. The equivalent circuit parameters are summarized in Table I. Fig. 3(a) shows the physical origins of the relevant equivalent circuit and parasitic components. The electromechanical motional behavior is represented

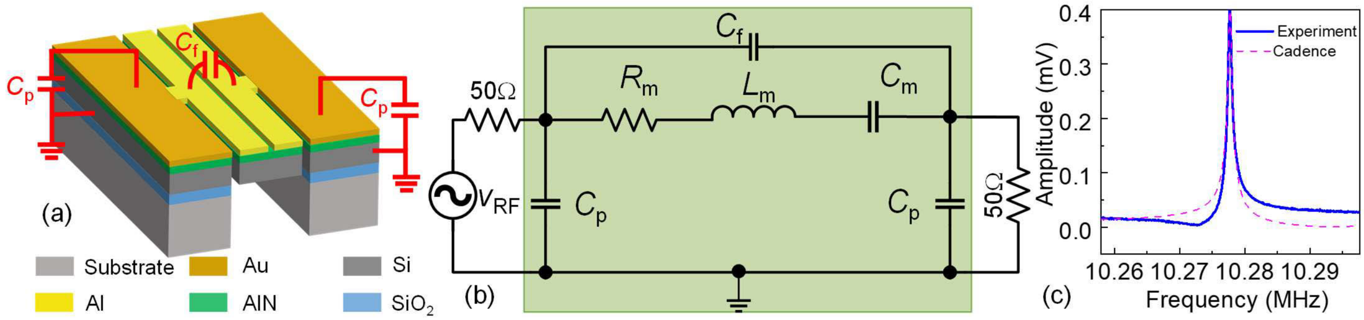

Fig. 3. (a) Illustration of physical origins of the relevant equivalent circuit and parasitic components. (b) Equivalent circuit model. (c) Fitting of experimental data using Cadence Virtuoso. The magenta dashed line shows simulated data using Cadence.

by R_m, L_m, and C_m, which can be calculated as

$$R_m = 2Z_0\left(10^{\frac{|\mathrm{IL}|}{20}} - 1\right) \quad (2)$$

$$L_m = \frac{Q(R_m + 2Z_0)}{2\pi f_0} \quad (3)$$

$$C_m = \frac{1}{L_m(2\pi f_0)^2} \quad (4)$$

where $Z_0 = 50\ \Omega$ is the terminal impedance of the measurement device (network analyzer) and IL is the measured insertion loss (magnitude of S_{21}) in dB.

The parasitic capacitor C_p is formed between the Au contact pad and the Si layer. It can be modeled as a parallel-plate capacitor $C_p = (\epsilon_r \epsilon_0\ A/d) = 2.75$ pF, where A is the area of the bottom surface of the contact pad, ϵ_0 is the permittivity of air, and $\epsilon_r = 8.9$ and d are the dielectric constant and thickness of the AlN layer, respectively. In addition, a feedthrough capacitor C_f is present between the input and output electrodes. The distance between the input and output electrodes is ~200 nm. We estimate $C_f \approx 250$ fF from simulations of the equivalent circuit model using Cadence (see Table I). Fig. 3(b) shows the circuit model of the resonator. The green square box shows the resonator portion of the equivalent circuit model. The fitting of experimental data using a circuit model of 10 MHz mode is demonstrated using a magenta dashed line in Fig. 3(c).

B. Characterization of Resonances

When an RF drive is applied to an electrode, the electric field induced in the piezoelectric AlN layer produces lateral stress at the same time due to the piezoelectric coefficient. Eventually, the stress field induces charge at the other electrode and the charge is sensed through the piezoelectric effect. We first measure the fundamental mode resonance of the piezoelectric resonator (10.28 MHz) by performing a two-port network analysis [see Fig. 4(a)]. At an RF drive level of $v_{\mathrm{RF}} =$ 100 mV, the device is still in the linear regime [see Fig. 4(b)]. Thus, the resonance data are analyzed by using the damped (finite-Q) simple harmonic resonator model

$$a = \left[\frac{\Gamma^2}{\left(\omega_0^2 - \omega^2\right)^2 + \left(\frac{\omega\omega_0}{Q}\right)^2}\right]^{1/2} + a_0 \quad (5)$$

TABLE I
SUMMARY OF DIFFERENT MODE PARAMETERS

Parameters	Mode 1	Mode 2	Mode 3	Mode 4	Mode 5
f_{osc} (MHz)	10.28	30.82	65.51	95.86	233.8
R_m (kΩ)	1.2	2.1	1.8	1.9	1.3
L_m (mH)	355	49	19.5	9.09	2.09
C_m (aF)	610	281	302	303	223
C_f (fF)	250	533	281	310	260
C_p (pF)	4	4	4	4	4
m_{eff} (kg)	3.9×10^{-10}	3.8×10^{-10}	3.5×10^{-10}	1.8×10^{-10}	4.4×10^{-11}
k_{eff} (N/m)	1.6×10^{6}	1.4×10^{7}	5.9×10^{7}	6.5×10^{7}	9.5×10^{7}
$\langle\delta m\rangle_{\tau_A=1}$ (fg)	6.1	193	3.96	25.5	0.85
$\langle\delta F\rangle$ (fN/Hz$^{1/2}$)	148	522	748	822	706

where a_0 represents a frequency-independent (flat) background due to electrical feedthrough, a is the measured amplitude, and Γ is a fitting parameter. Fitting of this model yields a quality factor of Q =18 600 [see Fig. 4(c)]. Next, we increase v_{RF} from 100 to 550 mV in 50 mV steps and observe the resonance peak frequency decreasing with increasing v_{RF}, displaying a softening Duffing nonlinearity [see Fig. 5(a)]. The experimental Duffing coefficient for this mode is $k_3 = -3.7 \times 10^5$ N/m^3 as obtained using the method described in [58]. The negative Duffing coefficient could be attributed to the softening of the equivalent Young's modulus due to the distributed material nonlinearity in Si and AlN [59]. Fig. 5(b) shows a bifurcation diagram for upward and downward frequency sweeps at $v_{\mathrm{RF}} =$ 400 mV drive with hysteresis clearly visible [60].

C. Calibration of Dynamic Range

We have been able to all-electrically measure the undriven thermomechanical noise spectrum of the 10 MHz mode, which is the first for this type of device (an AlN-on-Si resonator in its LE mode), as shown in Fig. 6(a) and (b). The resonator is always inherently interacting with its surroundings at finite temperatures, i.e., the surroundings act as a thermal bath in thermodynamic equilibrium with the resonator. Stochastic forces from random agitations of the thermal bath push the resonator into mechanical motion at constant temperature in thermodynamic equilibrium. At the same time, the stochastic forces also retard the motion of the resonator. This process, which is referred to as fluctuation–dissipation thermomechanical motion, shares the same fundamental physics as the Brownian motion [61], [62] and can be mathematically

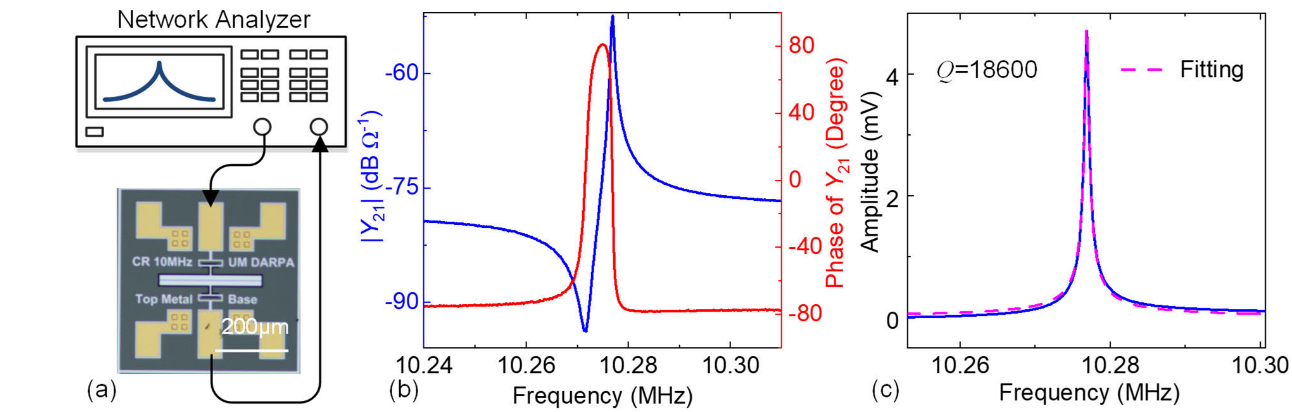

Fig. 4. (a) Illustration of measurement setup for all-electrical characterization of the AlN/Si resonator. (b) Magnitude and phase of the admittance parameter Y_{21} (where Y_{21} (dB Ω^{-1}) = 20 $\log_{10}(Y_{21}(\Omega^{-1}))$) converted from measured S-parameters in the linear regime for the 10 MHz mode. (c) Fitting of the resonance (magenta dashed line) using a damped (finite-Q) harmonic resonator model after background subtraction.

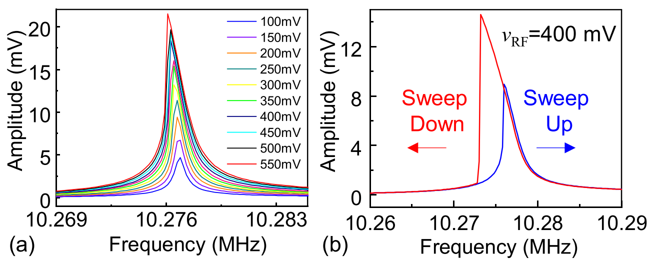

Fig. 5. (a) Electrically measured linear to nonlinear responses by increasing RF drive v_{RF} from 100 to 550 mV. (b) Nonlinear bifurcation curves with both upward (blue) and downward (red) frequency sweeps.

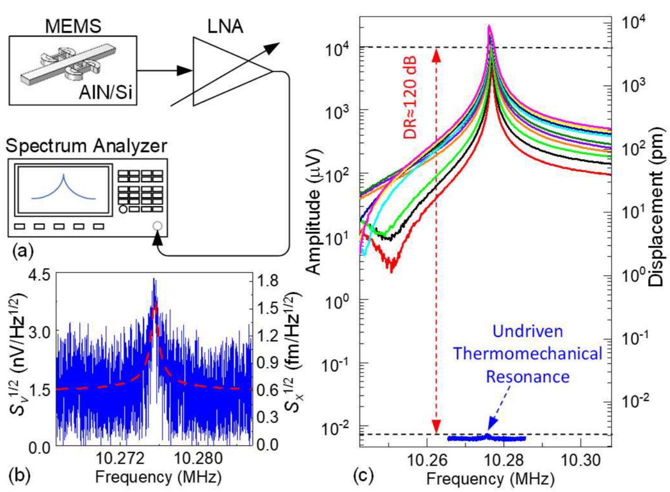

Fig. 6. (a) Scheme for high-precision electrical measurement of thermomechanical noise. (b) Electrically measured thermomechanical noise spectrum for the fundamental mode at 10 MHz. (c) Calibration of Duffing nonlinearity with thermomechanical noise for determination of DR.

described by a Langevin equation [61]. The thermomechanical motion of the MEMS resonator and its corresponding noise imposes a fundamental limit on the device performance (transduction and response).

In the frequency domain, the spectral density of the resonator's thermomechanical motion displacement can be written as [63]

$$S_{x,\mathrm{th}}^{1/2}(\omega) = \left[\frac{4\,\omega_0\,k_\mathrm{B}\,T}{Q\,m_\mathrm{eff}}\frac{1}{\left(\omega_0^2-\omega^2\right)^2+\left(\frac{\omega\,\omega_0}{Q}\right)^2}\right]^{1/2} \tag{6}$$

where k_B, T, m_eff, Q, and ω_0 are Boltzmann's constant, temperature, effective mass, quality factor, and angular resonance frequency, respectively. The value of m_eff is estimated from FEM in COMSOL for each mode. On resonance, (6) simplifies to

$$S_{x,\mathrm{th}}^{1/2}(\omega) = \left(\frac{4k_\mathrm{B}T\,Q}{\omega_0^3 m_\mathrm{eff}}\right)^{1/2}. \tag{7}$$

All-electrical calibration of thermomechanical noise has been attained by using the undriven AlN/Si MEMS resonator connected to a low-noise amplifier (LNA) [see Fig. 6(a)]. The output of the MEMS resonator is connected to the input of the LNA (Femto HVA-200M-40-F) [41], and the output of the amplifier is connected to the spectrum analyzer. We use the 20 dB gain setting of the LNA for this measurement. To obtain the thermomechanical noise of the resonator, we need to measure the noise floor of the amplifier and then refer everything to its input. Thus, we have measured the noise floor of the LNA by connecting its output (with 20 dB gain) to the spectrum analyzer with the input of the amplifier grounded. We assume that the noise sources are uncorrelated and subtract the LNA noise floor from that of the resonator and amplifier noise by using

$$S_{v,\mathrm{MEMS}}^{1/2} = \sqrt{\left(S_{v,\mathrm{MEMS+LNA}}^{1/2}\right)^2 - \left(S_{v,\mathrm{LNA}}^{1/2}\right)^2} \tag{8}$$

where $S_{v,\mathrm{MEMS}}^{1/2}$ is the thermomechanical noise of the resonator after calibration, $S_{v,\mathrm{MEMS+LNA}}^{1/2}$ is the thermal noise of both resonator and amplifier, and $S_{v,\mathrm{LNA}}^{1/2}$ is the amplifier noise floor. We note that both $S_{v,\mathrm{MEMS+LNA}}^{1/2}$ and $S_{v,\mathrm{LNA}}^{1/2}$ are referred to the input of the amplifier by dividing both the output $S_{v,\mathrm{MEMS+LNA}}^{1/2}$ and $S_{v,\mathrm{LNA}}^{1/2}$ by a factor of 10 (20 dB). From the measured and calculated thermomechanical noise, we obtain the device's displacement-to-voltage responsivity $\Re = 2.8\ \mu$V/pm. In addition, the red dashed line in Fig. 6(b) shows the best-fitting thermomechanical noise spectrum predicted by (6) after doing calibration.

The spectral density of thermomechanical motion, $S_{x,\text{th}}^{1/2}(\omega)$ can be integrated to obtain the noise floor of the resonator, which is required to experimentally determine its intrinsic dynamic range (DR) and power handling capability. The intrinsic upper limit of the DR is imposed by the maximum achievable vibration amplitude beyond which a bifurcation point can exist, and the device response experiences hysteresis [see Fig. 5(b)] [64]. In physics and mechanics, it is common to assume that nonlinearity begins abruptly right at the bifurcation. However, in engineering practice, the onset of nonlinearity is typically defined as the 1 dB compression point, which frequently produces more conservative estimates than using bifurcation. We can write the damped simple harmonic resonator model, including nonlinear terms as

$$m_{\text{eff}}\ddot{x} + \gamma_{\text{eff}}\dot{x} + k_{\text{eff}}x + k_3x^3 = F(t) \tag{9}$$

where $\gamma_{\text{eff}} = m_{\text{eff}}\omega_0/Q$ is the damping coefficient, $k_{\text{eff}} = m_{\text{eff}}{\omega_0}^2$ is the effective spring constant, and $F(t)$ is the driving force. The maximum achievable vibration amplitude is $0.745x_c$ at the resonator's 1 dB compression point, where x_c is defined as the critical displacement in rms units [65]. The intrinsic DR of the resonator is obtained by taking the ratio of this amplitude signal ceiling and the displacement noise floor imposed by the thermomechanical motion referred to the input of the amplifier, i.e.,

$$\text{DR} = 20\log\left[\frac{0.745x_\text{c}}{S_{x,\text{th}}^{1/2}\text{BW}^{1/2}}\right] \tag{10}$$

where BW is the measurement bandwidth (BW). The intrinsic RF power handling of the fundamental 10 MHz LE mode, defined by the onset of nonlinearity, is $P = \omega_0 k_{\text{eff}}x_c^2/Q$ $\approx$90 nW [66]. The estimated DR for this mode is 120 dB [see Fig. 6(c)].

III. Oscillator Characterization

A. Oscillator Using the 10-MHz Resonance Mode

We first perform open-loop measurements [see Fig. 7(a) and (b)] to satisfy the Barkhausen criteria [67], with the overall open-loop gain being slightly greater than 1 (0 dB) near the resonance frequency and an overall phase change of $2n\pi$, where n is an integer. After satisfying the Barkhausen criteria, we close the loop [see Fig. 8(a)] and characterize the stable self-oscillations in both frequency and time domains [see Fig. 8(b) and (c)]. The measurement results show near sinusoidal oscillations. The equipment used in the measurement for all modes is summarized in Table II.

B. Phase Noise and Allan Deviation of 10-MHz Oscillator

Next, we systematically characterized the specifications and performance of the 10 MHz oscillator (see also Fig. 1). First, we examine the phase noise performance using the dedicated phase noise analysis module in a spectrum analyzer [see

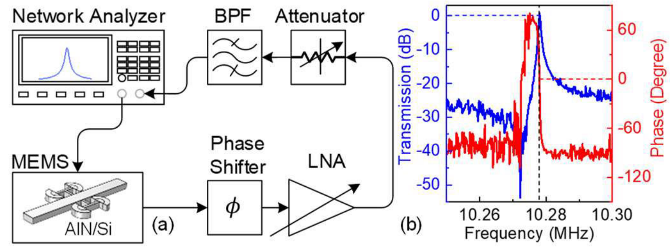

Fig. 7. (a) Scheme for open-loop characterization of the feedback oscillators. (b) Open-loop gain and phase calibration for making the 10-MHz oscillator.

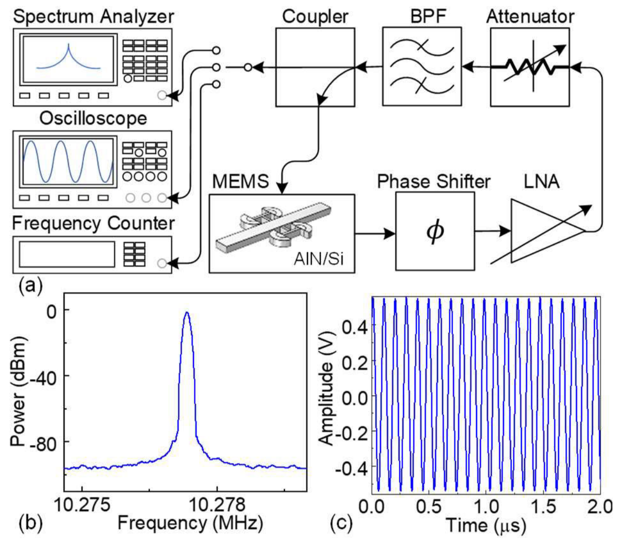

Fig. 8. (a) Measurement scheme for closed-loop characterization of the oscillators. (b) Frequency-domain output spectrum of the 10 MHz oscillator. (c) Time-domain output waveform of the 10 MHz oscillator.

Fig. 9(c)]. In wireless communication systems, low phase noise in reference oscillators is important because the close-in carrier phase noise increases the noise figure of the receiver by adding noise in receiver bandwidth. Phase noise is generally quantified as the sideband power spectral density (PSD) at an offset frequency Δf, normalized by the carrier power P_c, $\mathcal{L}(\Delta f) = 10\log\left[P_{\text{sideband}}(f_c + \Delta f)/P_c\right]$, with unit of dBc/Hz, where f_c is the carrier frequency [68], [69], [70], [71], [72]. The carrier frequency for the MEMS resonator is simply its resonance frequency, $f_c = f_0$. The phase noise of a weakly nonlinear oscillator can be often described by Leeson's model [68], [72]

$$\mathcal{L}(\Delta f) = 10\log\left[(2F_nk_\text{B}T/P_c).\left(1+\left(\frac{f_0}{2Q\Delta f}\right)^2\right).\left(1+\frac{f_{1/f^3}}{\Delta f}\right)\right] \tag{11}$$

where F_n is the equivalent noise factor, k_B is Boltzmann's constant, T is temperature, and f_{1/f^3} is the knee frequency. This model is simplified and does not always have good predictive power, but nevertheless is useful in understanding for decreasing phase noise. From (11), we can see that to design a low phase noise oscillator, we need to: 1) minimize the amplifier and resonator noise; 2) increase the carrier power P_c; and 3) maximize the resonator Q. The ultimate phase noise

TABLE II

List of Lab Equipment [41], [42], [43], [44], [45], [46], [47], [48], [49], [50], [51], [52], [53], [54], [55], [56], [57] Used During the Experiments

Mode	LNA	LNA Noise Floor (dBm)	Phase Shifter	Filter	Atten.	Coupler
1	Femto HVA-200M-40B [41]	-156	Mini-Circuits JSPHS-12+ [43]	Mini-Circuits SBP-10.7+ [48]	JFW 50DR -060 [57]	Mini-Circuits ZFDC-10-1-S+ [56]
2	Femto HVA-200M-40B	-156	Mini-Circuits SCPHS-51+ [44]	Mini-Circuits SHP-20+, BLP-30+ [49-50]		
3	Femto HVA-200M-40B	-156	Synergy Microwave PK-712S [45]	Mini-Circuits SBP-70+ [51]		
4	Femto HVA-200M-40B	-156	Mini-Circuits SCPHS-180+ [46]	Mini-Circuits SHP-100+, SLP-100+ [52-53]		
5	Miteq AU-3A-0150 [42]	-133	Mini-Circuits SPHSA-251+ [47]	Mini-Circuits SHP-250+, SLP-300+ [54-55]		

performance limit of an oscillator is set by: 1) the intrinsic thermomechanical fluctuations and 2) power handling level (or DR) of the MEMS resonance mode [67]. Specifically, Leeson's model predicts that

$$\mathcal{L}(\Delta f) = 10\,log\left[\left(\frac{k_B T}{2P_c Q^2}\right)(f_0/\Delta f)^2\right] \tag{12}$$

in the $1/f^2$ regime. Once $\mathcal{L}(\Delta f)$ is known, the usual figure of merit (FoM) of an oscillator can be calculated using [73]

$$\text{FoM}(\Delta f) = 20\log\left(\frac{f_0}{f}\right) - \mathcal{L}(\Delta f) - 10\log\left(\frac{P_{dc}}{1\text{mW}}\right) \tag{13}$$

where P_{DC} is the dc power consumption of the oscillator. However, we do not report the FoM in this article since our oscillators used off-the-shelf LNAs (as listed in Table II) that were not optimized for dc power consumption.

Phase noise can also be measured as frequency noise $S_{(\Delta f)}\Delta f$, as phase is the time integral of frequency. The relationship between phase noise and frequency noise is

$$\mathcal{L}(\Delta f) = (1/\Delta f)^2 S_{(\Delta f)}\Delta f. \tag{14}$$

Equation (14) shows us that the power law of the phase noise spectrum is two orders lower than that of the frequency noise. For example, white noise (flat) and flicker noise ($1/f$) are converted into $1/f^2$ and $1/f^3$ power laws in the phase noise spectrum, respectively.

From the measured result, we observe two distinct regions in the phase noise behavior [see Fig. 9(c)]. Close to the carrier frequency, the spectrum first follows a $1/f^3$ power law from 250 to 700 Hz, which suggests contributions from flicker noise. The spectrum flattens out at larger offset frequencies suggesting that the amplitude noise is dominant in this region. The measured phase noise data are empirically fit using Leeson's model [68], [72], which gives a $1/f$ (i.e., $1/f^3$ in phase noise) knee frequency of ~970 Hz and an equivalent noise factor of $F_n = 4$. The phase noise at 1 kHz offset (which is a common FoM for oscillators) is approximately −116 dBc/Hz. The ultimate phase noise limit imposed by thermomechanical noise and DR of this resonance mode is shown as the orange dashed line in Fig. 9(c). The measured phase noise is ~20–40 dB higher than the intrinsic limit in the 0.1−1 kHz offset frequency range due to: 1) extrinsic noise contributions from readout electronics and feedback circuitry and 2) frequency fluctuations in the resonator beyond its thermomechanical noise [74]. To clearly investigate the

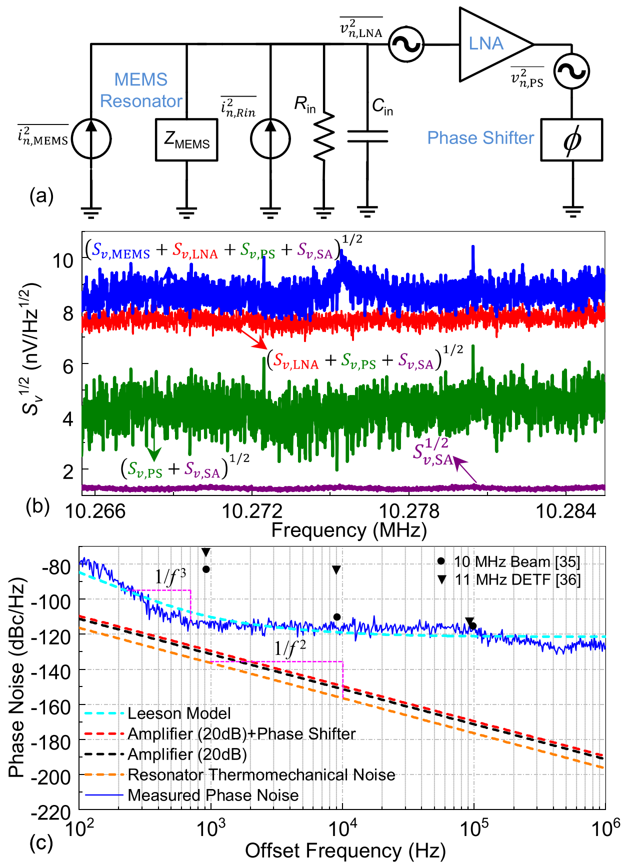

Fig. 9. Phase noise of the 10 MHz mode oscillator obtained after calibrating the noise level of the measurement system. (a) Simplified input-referred noise model for both voltage and current sensing. (b) Calibration of noise level of the measurement system. (c) Phase noise measured from the 10 MHz oscillator (blue) compared with 10 MHz beam [35] and 11 MHz DETF [36] resonators. The orange dashed line displays the thermomechanical noise limit of the MEMS resonator. The red dashed line shows the thermal noise limits of both Femto LNA and Mini-Circuits phase shifter. The black dashed line shows the thermal noise limits of the LNA (with 20 dB gain).

limitation of our active circuitry, we have carefully calibrated the noise level of the measurement system. First, we analyze the input-referred noise model of the measurement system. We consider the dominant sources of phase noise to be the LNA, phase shifter, and the MEMS resonator. A simplified input-referred noise model for both voltage- and current-sensing LNA is shown in Fig. 9(a). In the circuit model shown in Fig. 9(a), $\overline{i^2_{n,\text{MEMS}}}$ is the noise current source for the MEMS resonator, $\overline{v^2_{n,\text{LNA}}}$ is the input-referred noise voltage of the LNA, and $\overline{v_{n,\mathrm{PS}}^2}$ is the input-referred noise voltage of the phase shifter. The input impedance of the LNA can be modeled as $Z_{\mathrm{in}} = R_{\mathrm{in}}||(1/sC_{\mathrm{in}})$. For the Femto HVA-200M-40B LNA [41], the nominal values of R_{in} and C_{in} are 50 Ω and 12 pF, respectively. The peak of the PSD of MEMS resonator noise (thermomechanical noise) occurs near its resonance frequency and can be estimated from its motional resistance R_m. The input-referred voltage noise for the fundamental mode of the AlN/Si LE resonator is thus expected to be $(\overline{v_n^2})^{1/2} = (4kTR_{m1})^{1/2} = 4.3$ nV/Hz$^{1/2}$ at room temperature. Usually, the measured MEMS noise PSD is higher than the thermomechanical limit due to additional noise mechanisms, including thermoelastic damping, temperature fluctuations, and adsorption–desorption [13].

Fig. 9(b) summarizes the calibrated noise levels of the measurement system. In Fig. 9(b), $S_{v,\mathrm{SA}}^{1/2}$, $S_{v,\mathrm{PS}}^{1/2}$, and $S_{v,\mathrm{LNA}}^{1/2}$ show the measured noise floor of the spectrum analyzer, a phase shifter (Mini-Circuits JSPHS-12+) [43], and an LNA (Femto HVA-200M-40B) [41]. The measured noise floor of the phase shifter and spectrum analyzer is ∼4.5 nV/Hz$^{1/2}$, and for the LNA, the phase shifter and spectrum analyzer are ∼7.5 nV/Hz$^{1/2}$.

From the datasheet, the input-referred voltage noise of the LNA should be $(\overline{e_n^2})^{1/2} \approx 3.5$ nV/Hz$^{1/2}$. However, our measured results show a higher noise PSD of ∼5.7 nV/Hz$^{1/2}$. This increase is likely due to the LNA's current noise, which is known to be load-dependent. In fact, we can estimate the current noise as $(\overline{i_{n,\mathrm{MEMS}}^2})^{1/2} = ((\overline{v_n^2} - \overline{e_n^2}/R_m^2))^{1/2}$. For the 10 MHz mode, the measured current noise PSD is ∼3.7 pA/Hz$^{1/2}$, which is a fairly typical value for BJT-input LNAs designed to operate at low impedance levels (e.g., 50 Ω systems). The current noise PSDs for the other modes are similar; the measured values for the 2nd, 3rd, 4th, and 5th LE modes are 2.1, 2.4, 2.3, and 3.4 pA/Hz$^{1/2}$, respectively. The input-referred noise floor of the entire electronics chain (LNA, phase shifter, attenuator, and splitter) is dominated by the LNA, as expected, and has a measured value of 7.5 nV/Hz$^{1/2}$. This result is larger than the ON-resonance thermomechanical noise generated by the MEMS resonator, $S_{v,\mathrm{MEMS}}^{1/2}$ ∼4.1 nV/Hz$^{1/2}$.

The thermal noise of the electronics is larger than, but just about 2×, that of the MEMS resonator, they are both expected to contribute to the phase noise of the 10 MHz oscillator. Nevertheless, the phase noise of the 10 MHz oscillator is excellent, surpassing that of earlier oscillators based on ∼10 MHz Si beam resonators [35], 11 MHz DETF resonators [36], and ∼11 MHz Ni resonators [37], and therefore promising for ultralow-power timing and clock applications.

Next, we characterize the frequency stability (Allan deviation) [75], [76], [77] for this mode. For frequency-shift-based sensing applications, the frequency fluctuation noise sets the ultimate limit of detection sensitivity [74]. Finding the relationship between the rms fractional frequency shift and the Allan deviation carefully requires analysis of their definitions followed by comparison in the time domain. The instantaneous fractional frequency shift can be written as

$$y(t) = \frac{\delta f_0}{f_0} = \frac{f(t) - f_0}{f_0}. \tag{15}$$

The measured value of fractional frequency shift for the arbitrary ith time interval with averaging time τ_A is defined as

$$\overline{y}_i = \frac{1}{\tau_A}\int_{t_i}^{t_i+\tau_A} y(t)dt. \tag{16}$$

The rms fractional frequency shift is defined as

$$\frac{\delta f_0}{f_0} = \left\langle\left(\frac{f - f_0}{f_0}\right)\right\rangle^{1/2} = \frac{1}{f_0}\langle(F - f_0)\rangle^{1/2} \tag{17}$$

where $\langle\ldots\rangle$ denotes infinite time average or ideal ensemble average. For practical measurements, the rms fractional frequency shift is dependent on a final ensemble average as

$$\frac{\delta f_0}{f_0} \cong \left[\frac{1}{(N-1)}\sum_{i=1}^{N-1}\left(\frac{\overline{f}_{i+1} - \overline{f}_i}{f_0}\right)^2\right]^{1/2} \tag{18}$$

where $\overline{f}_i$ is the measured average frequency in the ith discrete time interval of τ_A. The rms value is dependent on sample standard deviation over the finite time interval.

The Allan variance is defined as the sample variance of two adjacent averages of the instantaneous fractional frequency shift, which is expressed as

$$\sigma_A^2(\tau_A) = \left\langle\left(\frac{\overline{y}_{i+1} - \overline{y}_i}{\sqrt{2}}\right)^2\right\rangle. \tag{19}$$

Thus, the Allan variance from a finite data ensemble for a real measurement can be written as

$$\sigma_A{}^2(\tau_A) = \frac{1}{2(N-1)}\sum_{i=1}^{N-1}\left(\frac{\overline{f}_{i+1} - \overline{f}_i}{f_0}\right)^2. \tag{20}$$

Since the Allan deviation is defined as the square root of Allan variance, it is written as

$$\sigma_A(\tau_A) = \left[\frac{1}{2(N-1)}\sum_{i=1}^{N-1}\left(\frac{\overline{f}_{i+1} - \overline{f}_i}{f_0}\right)^2\right]^{1/2}. \tag{21}$$

The frequency-domain phase noise and time-domain Allan deviation are correlated as

$$\sigma_A(\tau_A) = \frac{2\sqrt{2}}{(f_0\tau_A)}\left[\int_0^\infty \mathcal{L}(\Delta f)\left(\sin\frac{\Delta f\tau_A}{2}\right)^4 d(\Delta f)\right]^{1/2}. \tag{22}$$

Considering the frequency stability limit imposed by thermomechanical motion, we find that the Allan deviation has $\sigma_A(\tau_A) \sim \tau_A^{-1/2}$ dependency using (13) and (22)

$$\sigma_A(\tau_A) = \frac{1}{Q}\sqrt{\frac{\pi k_B T}{P_c\tau_A}}. \tag{23}$$

Similarly, we get $\sigma_A(\tau_A) \sim \tau_A^{1/2}$ for $1/f^2$ drifting frequency noise (for which the phase noise follows a $1/f^4$ power law) and $\sigma_A(\tau_A)$ independent of τ_A ($\sim\tau_A{}^0$) for $1/f$ frequency noise (for which phase noise follows a $1/f^3$ power law).

We measure the frequency fluctuations of the 10 MHz mode oscillator using a frequency counter in the closed-loop measurement scheme [see Fig. 8(a)]. From the raw data [long frequency traces, Fig. 10(a)], we compute the Allan deviation [see Fig. 10(b)] using (20). The computed Allan deviation

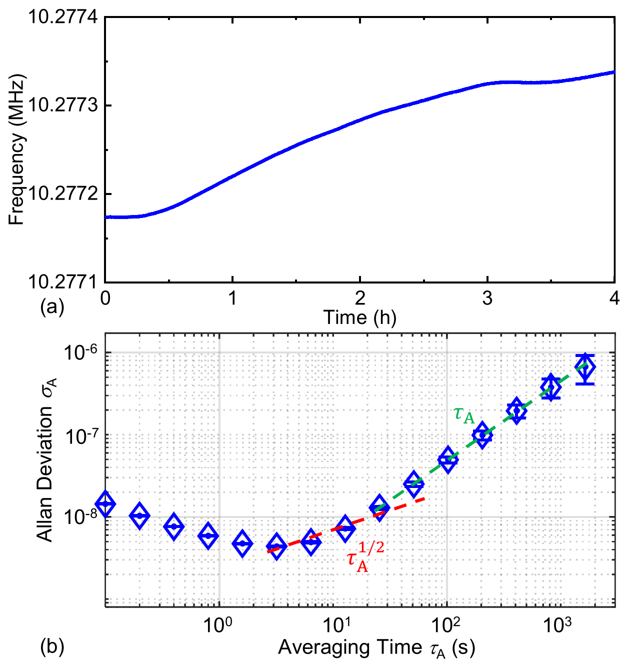

Fig. 10. (a) Measured long-trace frequency of the 10 MHz oscillator over 4 h. (b) Computed Allan deviation showing $\tau_A^{1/2}$ and τ_A^1 power laws.

data from frequency fluctuations gives us both the short-term stability ($\sigma_A \approx 5.5 \times 10^{-9}$ for an averaging time of $\tau_A = 1$ s) and long-term stability ($\sigma_A \approx 1 \times 10^{-6}$ for $\tau_A = 10^3$ s). The Allan deviation data follow a $\tau_A^{1/2}$ power law for short-term averaging (τ_A = 3–15 s) and follow a τ_A^1 power law for long-term averaging (τ_A = 25–2000 s). Our measured best Allan deviation of 5.5×10^{-9} at $\tau_A = 1$ s for this mode is smaller than for previously reported 10-MHz Si in-plane Lamé mode resonators [63]. Given this mode's effective mass $m_{\text{eff}} = 3.92 \times 10^{-10}$ kg and mass responsivity of $\Re_m = \omega_0/(2m_{\text{eff}}) = 0.08$ Hz/ag, a mass sensitivity (or resolution) of $\langle \delta m \rangle_{\tau_A} = 2m_{\text{eff}} \langle \delta f_0/f_0 \rangle_{\tau_A} = 6.1$ fg is achieved for short measurement times ($\tau_A = 1$ s) [78]. This mode also shows a high force sensitivity of $\langle \delta F \rangle = ((4k_B T m_{\text{eff}} \omega_0/Q))^{1/2} = 148$ fN/Hz$^{1/2}$ limited by its thermomechanical motion.

The correlation between frequency-domain phase noise and time-domain frequency stability (Allan deviation) can be understood from Figs. 9(c) and 10(b). While the white and flicker noise affect the short-term stability, the long-term stability is compromised by drift and aging performance.

C. Oscillator Using the 30 MHz Resonance Mode

We characterize [see Fig. 11(a)] the 2nd LE mode (30.82 MHz) by increasing v_{RF} from 100 mV to 1.2 V and obtain Q= 4350 [see Fig. 11(b)] by using the simple harmonic resonator model. Even at $v_{\text{RF}} = 1.2$ V (highest output voltage from the network analyzer), we find linear resonance for this mode. Thus, the 2nd LE mode has higher DR as well as RF power handling compared to the 1st LE mode. We measure both open-loop response [see Fig. 12(a)] and closed-loop oscillator performance [see Fig. 12(b)] using the same measurement method as used for the 10 MHz oscillator.

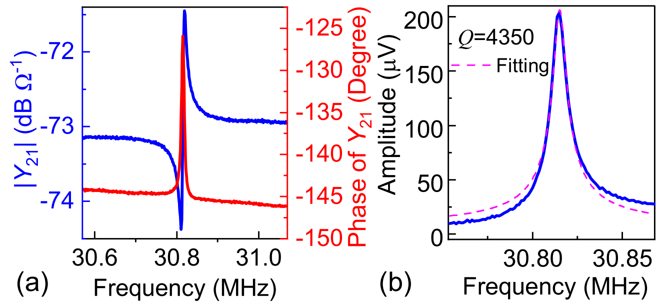

Fig. 11. (a) Magnitude and phase of the admittance parameter Y_{21} converted from measured S-parameters in the linear regime for the 30 MHz mode. (b) Fitting of the resonance using the damped (finite-Q) harmonic resonator model.

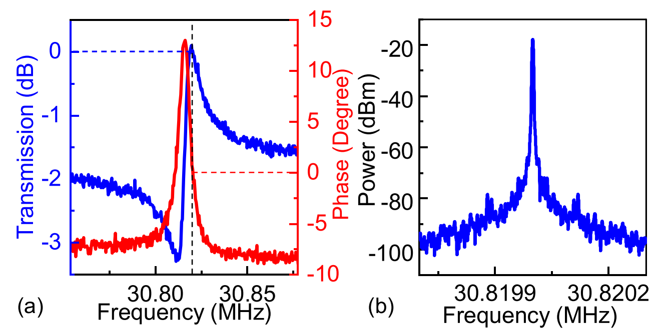

Fig. 12. (a) Open-loop gain and phase calibration for realizing the 30 MHz oscillator. (b) Measured output power spectrum of the 30 MHz oscillator.

D. Allan Deviation and Phase Noise of the 30 MHz Oscillator

We first compute the Allan deviation for this oscillator from frequency trace data recorded for 4 h [see Fig. 13(a) and (b)]. This 30 MHz oscillator has short-term stability σ_A (1 s) $\approx 1.8 \times 10^{-7}$ and long-term stability σ_A (10^3 s) $\approx 1.5 \times 10^{-6}$ [see Fig. 13(b)], better than the Si counterpart discussed in [79]. The Allan deviation data follow a $\tau_A^{1/2}$ power law for long-term averaging ($\tau_A = 10^2$–10^3 s). This mode has an effective mass $m_{\text{eff}} = 3.8 \times 10^{-10}$ kg and a mass responsivity $\Re_m = 0.25$ Hz/ag. We accordingly calculate a mass sensitivity (or resolution) of $\langle \delta m \rangle_{\tau_A} = 2m_{\text{eff}} \langle \delta f_0/f_0 \rangle_{\tau_A} =$ 193 fg for short measurement time ($\tau_A = 1$ s).

Next, we investigate the phase noise performance (see Fig. 14), following the same procedure as in Section III-B. Phase noise follows a $1/f^2$ power law over offset frequencies from 1 kHz to 1 MHz, suggesting that it is dominated by fluctuating sources with white spectra [69], [70]. This oscillator achieves a close-in carrier phase noise of −100 dBc/Hz (at 1 kHz offset) and far-from carrier phase noise of −160 dBc/Hz (at 1 MHz offset). The far-from carrier phase noise for this oscillator satisfies the 13 MHz GSM requirements [80]. The higher close-in carrier phase noise in this mode can be due to lower carrier power (−18 dBm), higher motional resistance (2.1 kΩ), and lower Q compared to the fundamental mode.

E. Oscillator Using the 65 MHz Resonance Mode

We further study the 3rd LE mode resonance (65.51 MHz) [see Fig. 15(a)] by increasing v_{RF} from 100 mV to 1.2 V and

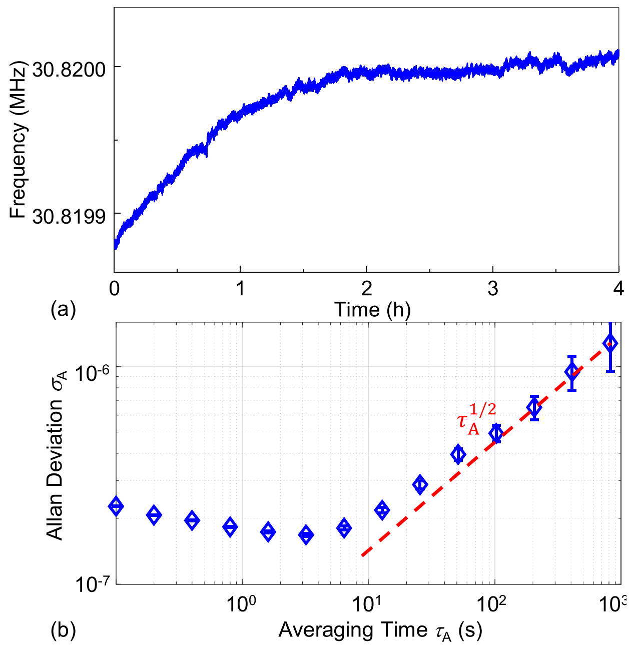

Fig. 13. (a) Measured long-trace frequency of the 30 MHz oscillator over 4 h. (b) Computed Allan deviation showing $\tau_A^{1/2}$ power law.

obtain Q= 4230 [see Fig. 15(b)] by using the simple harmonic resonator model. At v_{RF} = 1.2 V, the device motion is still in a linear regime similar to the 2nd LE mode. We measure both open-loop responses [see Fig. 16(a)] and closed-loop oscillator performance [see Fig. 16(b)] using the same measurement method as discussed for the fundamental mode. The closed-loop spectrum shows near sinusoidal oscillation with a carrier power near 0 dBm.

F. Allan Deviation and Phase Noise of the 65 MHz Oscillator

The frequency stability measured from the 65 MHz oscillator is impressive (see Fig. 17), which features the short-term Allan deviation of σ_A (1 s) $\approx 4 \times 10^{-9}$ and the long-term stability of σ_A (10^3 s) $\approx 2 \times 10^{-7}$, all at room temperature. These are the best frequency stability specifications achieved among our oscillators. The Allan deviation data follow a $\tau_A^{1/2}$ power law from $\tau_A = 12-100$ s and a τ_A^1 power law from $\tau_A = 200-1800$ s. Given this mode's effective mass $m_{\text{eff}} = 3.14 \times 10^{-10}$ kg and mass responsivity of $\Re_m = 0.104$ Hz/ag, a mass sensitivity (or resolution) of 3.55 fg is expected for short measurement time ($\tau_A = 1$ s). Even though this 3rd LE mode has high stiffness ($k_{\text{eff}} = 5.9 \times 10^7$ N/m), the oscillator referenced to it still offers an intrinsic force sensitivity of $\langle \delta F \rangle = 748$ fN/Hz$^{1/2}$ limited by thermomechanical motion.

The measured phase noise of this 3rd oscillator follows $1/f^3$ power law in the 120 Hz$-$1.2 kHz offset frequency range (suggesting contribution from flicker noise) and then flattens out (suggesting contributions from amplitude noise), and after that, it starts decreasing again (see Fig. 18). The phase noise is -105 dBc/Hz at a 1 kHz offset and -130 dBc/Hz at a 1 MHz offset. All these specifications are pretty good for a 65 MHz MEMS oscillator.

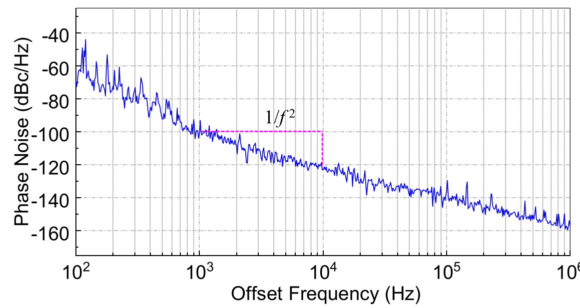

Fig. 14. Phase noise measured from the 30 MHz oscillator. The magenta dashed line shows $1/f^2$ power law.

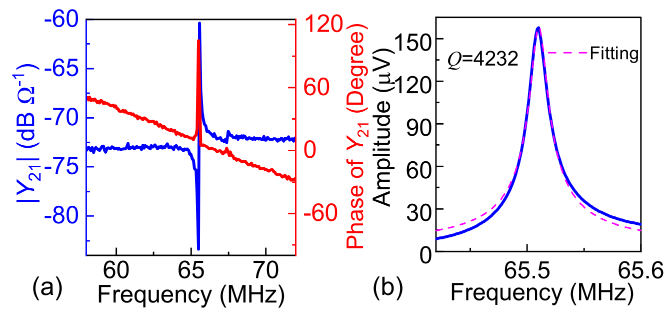

Fig. 15. (a) Magnitude and phase of the admittance parameter Y_{21} converted from measured S-parameters in the linear regime for the 65 MHz mode. (b) Fitting of the resonance using the damped (finite-Q) harmonic resonator model.

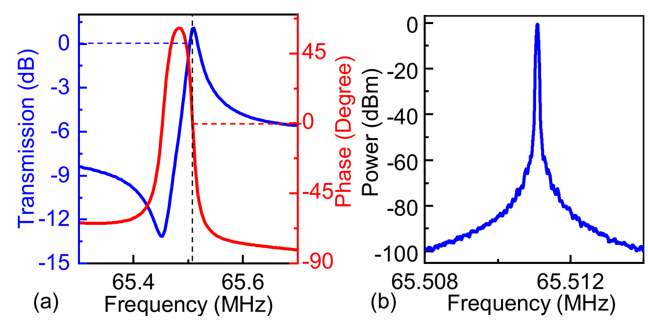

Fig. 16. (a) Open-loop gain and phase calibration for realizing the 65 MHz oscillator. (b) Measured output power spectrum of the 65 MHz oscillator.

G. Oscillator Using the 95 MHz Resonance Mode

We characterize the 4th LE mode resonance (95.82 MHz) [see Fig. 19(a)] by increasing v_{RF} from 0.1 to 1.2 V and obtain Q= 2630 [see Fig. 19(b)] by using the simple harmonic resonator model. Even at v_{RF} = 1.2 V, the device motion is still in a linear regime similar to the 2nd and 3rd LE modes. We measure both open-loop response [see Fig. 20(a)] and closed-loop oscillator performance [see Fig. 20(b)] using the same measurement method as discussed for the fundamental mode. The closed-loop spectrum is nearly sinusoidal but does exhibit unwanted spurs coming from spurious resonance modes.

H. Allan Deviation and Phase Noise of the 95 MHz Oscillator

We compute the Allan deviation from frequency trace data recorded for 4 h [see Fig. 21(a) and (b)]. The 95 MHz

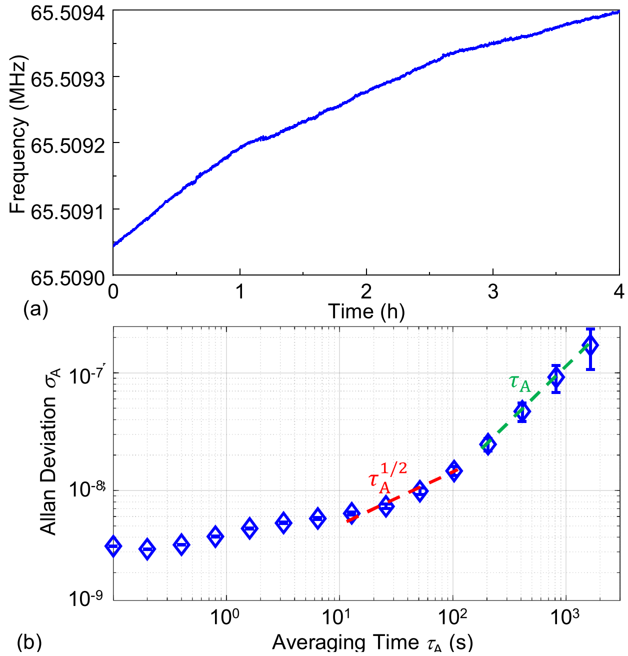

Fig. 17. (a) Measured long-trace frequency of the 65 MHz oscillator over 4 h. (b) Computed Allan deviation showing $\tau_A^{1/2}$ and τ_A^1 power laws.

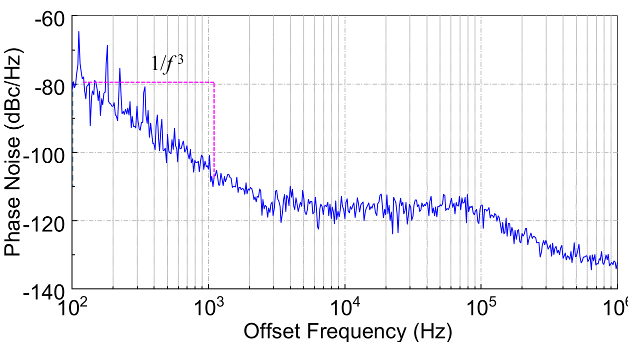

Fig. 18. Phase noise measured from the 65 MHz oscillator, which follows $1/f^3$ power law from 100 Hz to 1 kHz offset frequency.

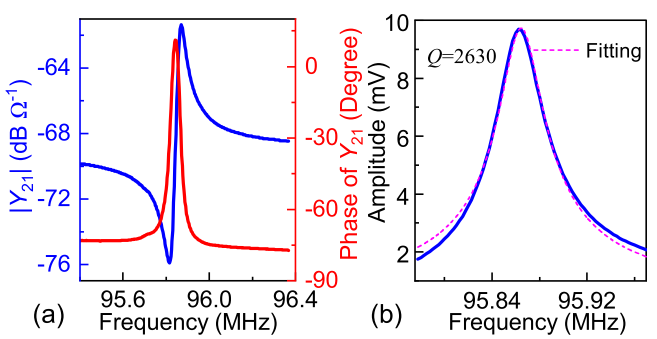

Fig. 19. (a) Magnitude and phase of the admittance parameter Y_{21} converted from measured S-parameters in the linear regime for the 95 MHz mode. (b) Fitting of resonance using the damped (finite-Q) harmonic resonator model.

oscillator has the short-term stability σ_A (1 s) $\approx 5 \times 10^{-8}$ and the long-term stability σ_A (10^3 s) $\approx 1.2 \times 10^{-7}$ [see Fig. 21(b)]. The Allan deviation data follow a $\tau_A^{-1/2}$ power law for very short averaging time (τ_A = 0.1–0.4 s). This mode has effective mass $m_{\mathrm{eff}} = 1.802 \times 10^{-10}$ kg and mass responsivity $\Re_m = 1.66$ Hz/zg. We calculate a mass sensitivity

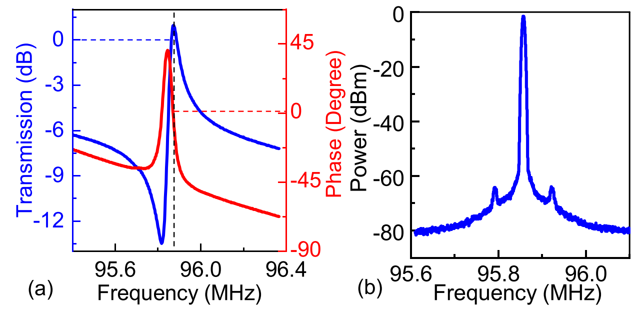

Fig. 20. (a) Open-loop gain and phase calibration for realizing the 95 MHz oscillator. (b) Measured output power spectrum of the 95 MHz oscillator.

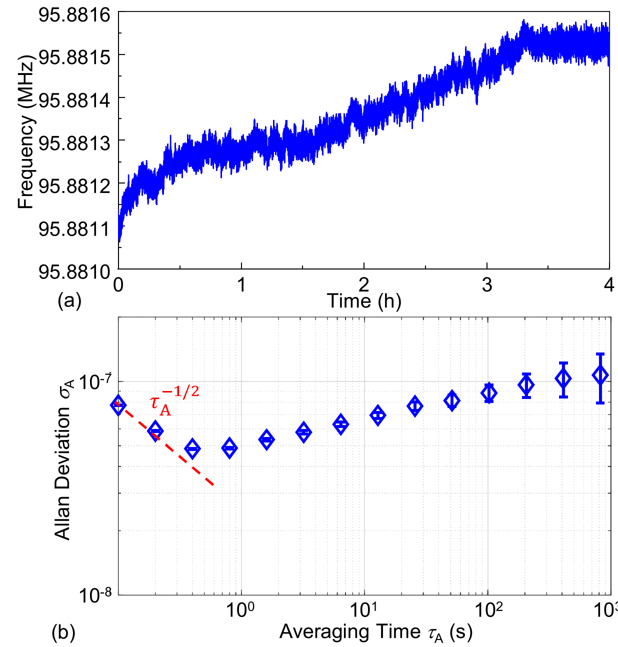

Fig. 21. (a) Measured frequency trace of the 95 MHz oscillator over 4 h. (b) Computed Allan deviation showing $\tau_A^{-1/2}$ power law.

(or resolution) of 25.5 fg for short measurement time (τ_A = 1 s) for this oscillator mode.

Next, we investigate the phase noise performance (see Fig. 22), following the same procedure as in earlier sections. The phase noise of this oscillation mode follows a $1/f^3$ power law from 0.1 to 1 kHz range suggesting contribution from flicker noise. It is dominated by amplitude noise from 6 to 10 kHz. We measure a close-in carrier phase noise of −106 dBc/Hz at 1 kHz offset (which is lower than previously reported ∼100 MHz AlN contour-mode resonator-based oscillators [81]) and far-from carrier phase noise of −132 dBc/Hz at 1 MHz offset. These are pretty good for a 95 MHz oscillator.

I. Oscillator Using the 233-MHz Resonance Mode

Finally, we characterize the 5th LE mode resonance (233.84 MHz) [see Fig. 23(a)] by increasing v_{RF} from 0.1 to 1.2 V and obtain Q= 2138. At v_{RF} = 1.2 V, we find linear resonance for this mode similar to the 2nd, 3rd, and 4th LE

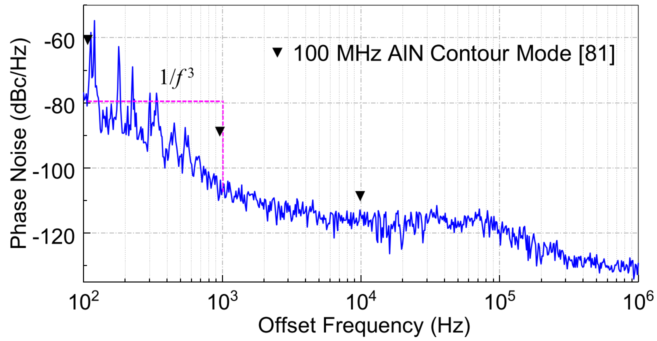

Fig. 22. Phase noise measured from the 95 MHz oscillator compared with [81], which follows $1/f^3$ power law from 100 Hz to 1 kHz offset frequency.

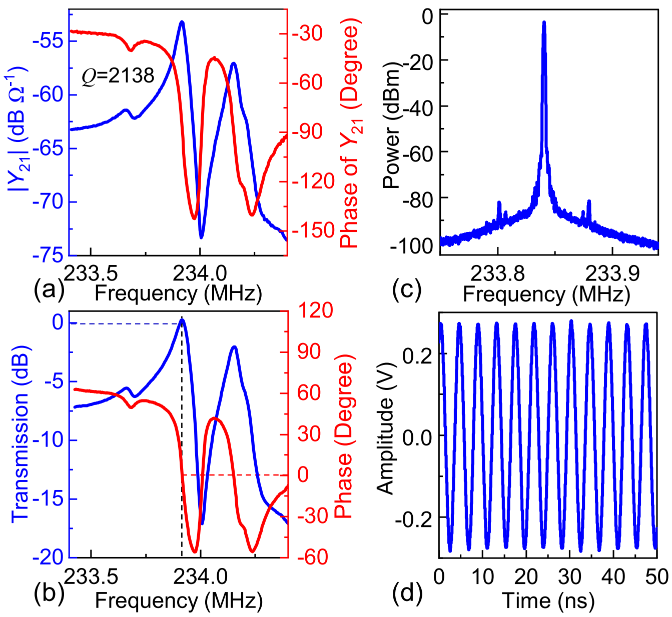

Fig. 23. (a) Magnitude and phase of the admittance parameter Y_{21} converted from measured S-parameters in the linear regime for the 233 MHz mode. (b) Open-loop gain and phase calibration for realizing the 233 MHz oscillator. (c) Measured output power spectrum. (d) Time-domain oscillation of the 233 MHz oscillator.

modes. There exists another resonance mode (234.2 MHz) near the 5th LE mode. We carefully calibrate the open-loop response so that the Barkhausen criteria are only satisfied for the 5th LE mode at 233.8 MHz. The open-loop responses [see Fig. 23(b)] and closed-loop oscillator performance [see Fig. 23(c) and (d)] are measured in the same measurement method as discussed in earlier sections. We use Miteq AU-3A-0150 low-noise amplifier [42] and Mini-Circuits SPHSA-251+ phase shifter [47] for this oscillator characterization. The closed-loop spectrum shows a carrier power near −3 dBm.

J. Allan Deviation and Phase Noise of 233 MHz Oscillator

For the 233 MHz oscillator, we first compute the Allan deviation from frequency trace data recorded for 4 h [see Fig. 24(a) and (b)]. The oscillator has the short-term stability of σ_A (1 s) $\approx 6.8 \times 10^{-9}$ and the long-term stability of σ_A (10^3 s) $\approx 2.5 \times 10^{-7}$ [see Fig. 24(b)]. The Allan deviation data remain constant (follows a τ_A^0 power law) for short averaging time ($\tau_A = 0.1$–1 s) and follows a τ_A^1 power law for long averaging times ($\tau_A = 50$–900 s). Given this mode's effective mass $m_{\mathrm{eff}} = 4.43 \times 10^{-11}$ kg and mass responsivity $\Re_m =$

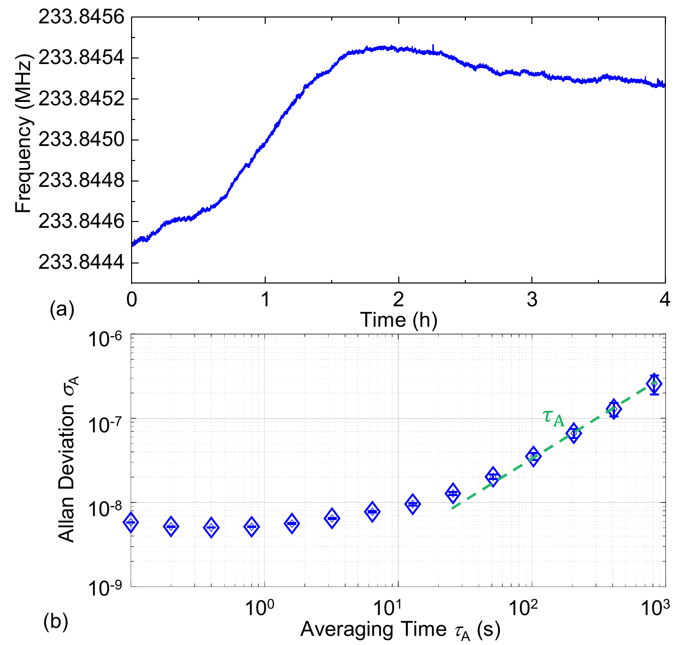

Fig. 24. (a) Measured long-trace frequency of the 233 MHz oscillator over 4 h. (b) Allan deviation computed from frequency trace largely follows τ_A^1 power law for long averaging time.

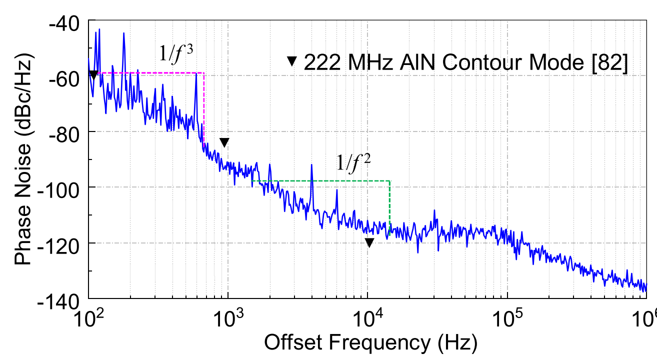

Fig. 25. Phase noise measured from the 233 MHz oscillator compared with [82]. The magenta and green dashed lines show $1/f^3$ and $1/f^2$ power laws, respectively.

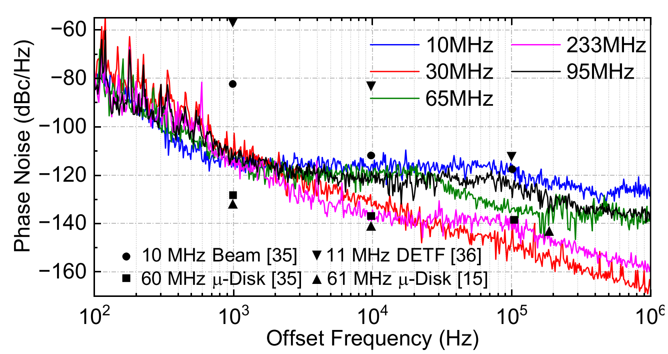

Fig. 26. Phase noise of all five oscillators benchmarked against previously reported electrostatic MEMS oscillators [15], [35], [36].

TABLE III
BENCHMARKING OF PHASE NOISE AND FREQUENCY STABILITY (ALLAN DEVIATION)

Reference	Resonator	Frequency (MHz)	Q	Number of Resonators	Carrier Power (dBm)	Phase Noise (dBc/Hz)			Best Allan Deviation, σ_A
						10^3Hz	10^5Hz	10^6Hz	
[35]	CC-Beam	10	8.61k	1	-20	-80	-120	-120	-
[36]	DETF	11	-	1	-17	-60	-110	-110	-
[37]	Ni	10.92	1.65k	1	-	-80	-90	-90	-
[83]	Dual Mode: Lamé & Torsional	20.2	950k	1	-	-	-	-	6.5×10^{-10} for $\tau_A=10^3$s
		1.16	770k		-	-	-	-	
	Dual Mode DETF	0.98	18k	1	-	-	-	-	1.2×10^{-9} for $\tau_A=10^3$s
		0.47	13k		-	-	-	-	
[79]	Si Nanowire	20	10k	1	-	-	-	-	1.5×10^{-6} for $\tau_A=1$s
[85]	AlN Micro-cantilever	0.09	125	1	-	-	-	-	1×10^{-8} for $\tau_A=10$s
[86]	AlN Contour Mode	220	1.40k	1	-	-	-	-	9×10^{-8} for $\tau_A=0.1$s
[87]	Si In-Plane Lamé	10.7	825k	1	-	-	-	-	1×10^{-8} for $\tau_A=10$s
[38]	BAW	30	3.85k	1	-	-70	-120	-130	-
		87	1.52k						
[81]	AlN Contour Mode	100	1.26k	3	-1.6	-90	-110	-125	-
[82]	AlN Contour Mode	176	1.50k	4	-4.7	-79	-	-	-
		222	2.10k		-4.8	-88	-150	-160	-
		306	1.40k		-6.7	-84	-	-	-
		482	0.85k		-13.6	-68	-	-	-
[88]	$LiNbO_3$ LOBAR	300-500	2.1k	1	0	-100	-148	-153	-
This Work	AlN/Si LE Mode	10.8	18.6k	1	-1	-116	-119	-120	5.5×10^{-9} for $\tau_A=1$s
This Work		30.8	4.35k		-18	-100	-140	-150	1.8×10^{-7} for $\tau_A=1$s
This Work		65.5	4.23k		-1	-105	-120	-130	4.0×10^{-9} for $\tau_A=1$s
This Work		95.8	2.63k		-2	-106	-120	-132	5.0×10^{-8} for $\tau_A=1$s
This Work		233.3	2.14k		-6	-92	-120	-138	6.8×10^{-9} for $\tau_A=1$s

16.52 Hz/ag, we calculate a mass sensitivity (or resolution) of $\langle\delta m\rangle_{\tau_A} = 0.85$ fg for short measurement time ($\tau_A = 1$ s). This is the best mass sensitivity achieved among all five oscillators.

We also investigate the phase noise performance (see Fig. 25), following the same procedure as in earlier sections. Phase noise follows a $1/f^3$ power law from 100 to 700 Hz suggesting contribution from flicker noise and follows a $1/f^2$ power law from 1.5 to 15 kHz, suggesting that this region is dominated by thermal noise. The measured phase noise is -92 dBc/Hz at 1 kHz offset and -138 dBc/Hz at 1 MHz offset. This oscillator's close-in carrier phase noise at a 1 kHz offset is lower than that of the earlier 222 MHz AlN contour-mode resonator [82].

IV. Performance Summary and Benchmarking

For a fair comparison, the phase noise data of all oscillators have been properly scaled to a 10 MHz carrier frequency. From this plot (see Fig. 26), we can observe that the phase noise of all our five oscillators (referenced to the five LE modes) surpasses the performance of earlier oscillators based on ∼10 MHz Si beam [35] and 11 MHz DETF resonators [36]. Thus, it is promising for ultralow-power timing and clock applications.

The best Allan deviation reported for MEMS resonators is 1.5×10^{-9} for a dual Lamé mode resonator [83] with complicated temperature compensation and ovenization. This device was also encapsulated using SiTime's very-high-temperature (∼1100 °C) Epi-Seal technology [84]. In contrast, our AlN/Si LE multimode oscillators show impressive stability even in everyday lab conditions without any special temperature control, compensation, or packaging. Specifically, the measured Allan deviation of the 10, 65, and 233 MHz oscillators surpasses various MEMS/NEMS oscillators reported to date. Furthermore, the Allan deviation data for these modes are approximately one order of magnitude lower than the previously reported piezoelectric MEMS/NEMS oscillators. Table III summarizes the phase noise and Allan deviation of all five oscillators and compares them with earlier work in this frequency range.

V. Conclusion

In summary, we have demonstrated five stable self-sustaining feedback oscillators (clocks) with clock frequencies at ∼10, 30, 65, 95, and 233 MHz, referenced to five high-Q LE modes of a single piezoelectric AlN/Si MEMS resonator. All the five oscillators exhibit high performance and impressive frequency stability, surpassing various MEMS/NEMS oscillators reported to date. The 10 MHz oscillator has better phase noise performance (-116 dBc/Hz at 1 kHz offset) than earlier counterparts with capacitive transduction. Due to low phase noise, these oscillators hold great potential for next-generation single-chip multifrequency RF transceivers. All five oscillators also clearly demonstrate strong potential for real-time multimode resonant sensing and inertial imaging, with best frequency stability measured by the Allan deviation down to 10^{-9} level. Future work includes heterointegration of AlN/Si MEMS resonators with a CMOS ASIC to realize a fully integrated multimode oscillator system-in-package (SiP).

References

[1] A. Ramezany and S. Pourkamali, "Ultrahigh frequency nanomechanical piezoresistive amplifiers for direct channel-selective receiver front-ends," *Nano Lett.*, vol. 18, no. 4, pp. 2551–2556, Apr. 2018.

[2] K. Jensen, J. Weldon, H. Garcia, and A. Zettl, "Nanotube radio," *Nano Lett.*, vol. 7, no. 11, pp. 3508–3511, 2007.

[3] A. Tazzoli, M. Rinaldi, C. Zuo, N. Sinha, J. Van Der Spiegel, and G. Piazza, "Aluminum nitride reconfigurable RF-MEMS front-ends," in *Proc. 9th IEEE Int. Conf. ASIC*, Xiamen, China, Oct. 2011, pp. 1046–1049.

[4] M. Rinaldi, C. Zuniga, C. Zuo, and G. Piazza, "Ultra-thin super high frequency two-port ALN contour-mode resonators and filters," in *Proc. Int. Solid-State Sensors, Actuat. Microsyst. Conf.*, Denver, CO, USA, Jun. 2009, pp. 577–580.

[5] Y. Shim, Z. Wu, and M. Rais-Zadeh, "A high-performance continuously tunable MEMS bandpass filter at 1 GHz," *IEEE Trans. Microw. Theory Techn.*, vol. 60, no. 8, pp. 2439–2447, Aug. 2012.

[6] A. Ozgurluk, M. Akgul, and C. T.-C. Nguyen, "RF channel-select micromechanical disk filters—Part I: Design," *IEEE Trans. Ultrason., Ferroelectr., Freq. Control*, vol. 66, no. 1, pp. 192–217, Jan. 2019.

[7] M. Rinaldi, C. Zuo, J. Van der Spiegel, and G. Piazza, "Reconfigurable CMOS oscillator based on multifrequency AlN contour-mode MEMS resonators," *IEEE Trans. Electron Devices*, vol. 58, no. 5, pp. 1281–1286, May 2011.

[8] B. Razavi, *Monolithic Phase-Locked Loops and Clock Recovery Circuits: Theory and Design*. Piscataway, NJ, USA: IEEE Press, 1996.

[9] M. S. Islam et al., "A programmable sustaining amplifier for flexible multimode MEMS-referenced oscillators," *IEEE Trans. Circuits Syst. I, Reg. Papers*, vol. 66, no. 4, pp. 1405–1418, Apr. 2019.

[10] Y. He et al., "A 673 μW 1.8-to-2.5 GHz dividerless fractional-N digital PLL with an inherent frequency-capture capability and a phase-dithering spur mitigation for IoT applications," in *IEEE Int. Solid-State Circuits Conf. (ISSCC) Dig. Tech. Papers*, San Francisco, CA, USA, Feb. 2017, pp. 420–421.

[11] J. Zarate-Roldan et al., "0.2-nJ/b fast start-up ultralow power wireless transmitter for IoT applications," *IEEE Trans. Microw. Theory Techn.*, vol. 66, no. 1, pp. 259–272, Jan. 2018.

[12] C. T.-C. Nguyen, "MEMS technology for timing and frequency control," *IEEE Trans. Ultrason., Ferroelectr., Freq. Control*, vol. 54, no. 2, pp. 251–270, Feb. 2007.

[13] M. S. Islam, S. K. Singh, G. Xereas, V. P. Chodavarapu, and S. Mandal, "A digitally programmable CMOS feedback ASIC for highly stable MEMS-referenced oscillators," *IEEE Trans. Circuits Syst. I, Reg. Papers*, vol. 66, no. 11, pp. 4158–4171, Nov. 2019.

[14] F. Ayazi, "MEMS for integrated timing and spectral processing," in *Proc. IEEE Custom Integr. Circuits Conf.*, San Jose, CA, USA, Sep. 2009, pp. 65–72.

[15] T. L. Naing, T. O. Rocheleau, E. Alon, and C. T.-C. Nguyen, "Low-power MEMS-based pierce oscillator using a 61-MHz capacitive-gap disk resonator," *IEEE Trans. Ultrason., Ferroelectr., Freq. Control*, vol. 67, no. 7, pp. 1377–1391, Jul. 2020.

[16] V. Kaajakari, T. Mattila, A. Oja, J. Kiihamaki, and H. Seppa, "Square-extensional mode single-crystal silicon micromechanical resonator for low-phase-noise oscillator applications," *IEEE Electron Device Lett.*, vol. 25, no. 4, pp. 173–175, Apr. 2004.

[17] (2018). *SiT5356 1 to 60 MHz, +/-0.1 to +/-0.25 ppm Elite Platform Precision Super-TCXO Datasheet*. [Online]. Available: https://www.sitime.com/support/resource-library/datasheets/sit5356-datasheet

[18] K. Jensen, K. Kim, and A. Zettl, "An atomic-resolution nanomechanical mass sensor," *Nature Nanotechnol.*, vol. 3, no. 9, pp. 533–537, Sep. 2008.

[19] B. Lassagne, D. Garcia-Sanchez, A. Aguasca, and A. Bachtold, "Ultrasensitive mass sensing with a nanotube electromechanical resonator," *Nano Lett.*, vol. 8, no. 11, pp. 3735–3738, Nov. 2008.

[20] K. L. Ekinci, X. M. H. Huang, and M. L. Roukes, "Ultrasensitive nanoelectromechanical mass detection," *Appl. Phys. Lett.*, vol. 84, no. 22, pp. 4469–4471, May 2004.

[21] B. Ilic, Y. Yang, and H. G. Craighead, "Virus detection using nanoelectromechanical devices," *Appl. Phys. Lett.*, vol. 85, no. 13, pp. 2604–2606, Sep. 2004.

[22] B. Ilic, Y. Yang, K. Aubin, R. Reichenbach, S. Krylov, and H. G. Craighead, "Enumeration of DNA molecules bound to a nanomechanical oscillator," *Nano Lett.*, vol. 5, no. 5, pp. 925–929, May 2005.

[23] Y. T. Yang, C. Callegari, X. L. Feng, K. L. Ekinci, and M. L. Roukes, "Zeptogram-scale nanomechanical mass sensing," *Nano Lett.*, vol. 6, no. 4, pp. 583–586, Apr. 2006.

[24] M. Nishio, S. Sawaya, S. Akita, and Y. Nakayama, "Carbon nanotube oscillators toward zeptogram detection," *Appl. Phys. Lett.*, vol. 86, no. 13, Mar. 2005, Art. no. 133111.

[25] A. K. Naik, M. S. Hanay, W. K. Hiebert, X. L. Feng, and M. L. Roukes, "Towards single-molecule nanomechanical mass spectrometry," *Nature Nanotechnol.*, vol. 4, no. 7, pp. 445–450, Jun. 2009.

[26] H.-Y. Chiu, P. Hung, H. W. C. Postma, and M. Bockrath, "Atomic-scale mass sensing using carbon nanotube resonators," *Nano Lett.*, vol. 8, no. 12, pp. 4342–4346, Dec. 2008.

[27] J. E. Sader, M. S. Hanay, A. P. Neumann, and M. L. Roukes, "Mass spectrometry using nanomechanical systems: Beyond the point-mass approximation," *Nano Lett.*, vol. 18, no. 3, pp. 1608–1614, Mar. 2018.

[28] M. S. Hanay et al., "Single-protein nanomechanical mass spectrometry in real time," *Nature Nanotechnol.*, vol. 7, no. 9, pp. 602–608, Sep. 2012.

[29] J. Chaste, A. Eichler, J. Moser, G. Ceballos, R. Rurali, and A. Bachtold, "A nanomechanical mass sensor with yoctogram resolution," *Nature Nanotechnol.*, vol. 7, no. 5, pp. 301–304, May 2012.

[30] S. Olcum, N. Cermak, S. C. Wasserman, and S. R. Manalis, "High-speed multiple-mode mass-sensing resolves dynamic nanoscale mass distributions," *Nature Commun.*, vol. 6, no. 1, p. 7070, May 2015.

[31] M. S. Hanay, S. I. Kelber, C. D. O'Connell, P. Mulvaney, J. E. Sader, and M. L. Roukes, "Inertial imaging with nanomechanical systems," *Nature Nanotechnol.*, vol. 10, no. 4, pp. 339–344, Apr. 2015.

[32] S. Dohn, W. Svendsen, A. Boisen, and O. Hansen, "Mass and position determination of attached particles on cantilever based mass sensors," *Rev. Sci. Instrum.*, vol. 78, no. 10, pp. 1–12, Oct. 2007.

[33] H. Jia and P. X.-L. Feng, "Tracing and resolving microparticle aquatic mass motion and distribution on multimode silicon carbide microdisk resonators," in *Proc. IEEE 32nd Int. Conf. Micro Electro Mech. Syst. (MEMS)*, Jan. 2019, pp. 529–532.

[34] T. Kaisar et al., "Multiple stable oscillators referenced to the same multimode AlN/Si MEMS resonator with mode-dependent phase noise and frequency stability," in *IEDM Tech. Dig.*, San Francisco, CA, USA, Dec. 2022, pp. 16.3.1–16.3.4.

[35] Y.-W. Lin, S. Lee, S.-S. Li, Y. Xie, Z. Ren, and C. T.-C. Nguyen, "Series-resonant VHF micromechanical resonator reference oscillators," *IEEE J. Solid-State Circuits*, vol. 39, no. 12, pp. 2477–2491, Dec. 2004.

[36] J. Verd, A. Uranga, J. Segura, and N. Barniol, "A 3V CMOS-MEMS oscillator in 0.35μm CMOS technology," in *Proc. 17th Int. Conf. Solid-State Sensors, Actuators Microsyst.*, Barcelona, Spain, Jun. 2013, pp. 806–809.

[37] W.-L. Huang, Z. Ren, Y.-W. Lin, H.-Y. Chen, J. Lahann, and C. T.-C. Nguyen, "Fully monolithic CMOS nickel micromechanical resonator oscillator," in *Proc. IEEE 21st Int. Conf. Micro Electro Mech. Syst.*, Tuscon, AZ, USA, Jan. 2008, pp. 10–13.

[38] M. J. Dalal, J. L. Fu, and F. Ayazi, "Simultaneous dual-mode excitation of piezo-on-silicon micromechanical oscillator for self-temperature sensing," in *Proc. IEEE 24th Int. Conf. Micro Electro Mech. Syst.*, Jan. 2011, pp. 489–492.

[39] S M E. H. Yousuf, Y. Liu, X.-Q. Zheng, A. Qamar, M. Rais-Zadeh, and P. X.-L. Feng, "Retaining high Q factors in electrode-less Aln-on-Si bulk mode resonators with non-contact electrical drive," in *Proc. IEEE 35th Int. Conf. Micro Electro Mech. Syst. Conf. (MEMS)*, Tokyo, Japan, Jan. 2022, pp. 979–982.

[40] A. Qamar, S. Sherrit, X.-Q. Zheng, J. Lee, P. X.-L. Feng, and M. Rais-Zadeh, "Study of energy loss mechanisms in AlN-based piezoelectric length extensional-mode resonators," *J. Microelectromech. Syst.*, vol. 28, no. 4, pp. 619–627, Aug. 2019.

[41] *FEMTO HVA-200M-40-B 200 MHz Low-Noise Amplifier Datasheet*. pp. 1–2. [Online]. Available: https://www.femto.de/en/products/voltage-amplifiers/10-mhz-200-mhz-or-500-mhz-hva.html

[42] *MITEQ-AU-3A-0150 RF Amplifier With Frequency 0.3 to 500 MHz Datasheet*. pp. 1–4. [Online]. Available: https://nardamiteq.com/docs/AU-3A-0150.pdf

[43] *Mini-Circuits JSPHS-12+ Phase Shifter Datasheet*. p. 1. [Online]. Available: https://www.minicircuits.com/pdfs/JSPHS-12+.pdf

[44] *Mini-Circuits SCPHS-51+ Phase Shifter Datasheet*. pp. 1–2. [Online]. Available: https://www.minicircuits.com/pdfs/SCPHS-51+.pdf

[45] *Synergy Microwave PK-712S Phase Shifter Datasheet*. pp. 1–2. [Online]. Available: https://www.datasheetarchive.com/PK-712-datasheet.html

[46] *Mini-Circuits SCPHS-180+ Phase shifter Datasheet*. pp. 1–2. [Online]. Available: https://www.minicircuits.com/pdfs/SCPHS-180+.pdf

[47] *Mini-Circuits SCPHS-251+ Phase Shifter Datasheet*. pp. 1–2. [Online]. Available: https://www.mini-circuits.com/pdfs/SPHSA-251+.pdf

[48] *Mini-Circuits SBP-10.7+ Band-Pass Filter Datasheet*. p. 1. [Online]. Available: https://www.minicircuits.com/pdfs/SBP-10.7+.pdf

[49] *Mini-Circuits SHP-20+ High-Pass Filter Datasheet*. pp. 1–3. [Online]. Available: https://www.mouser.com/datasheet/2/1030/SHP_20_2b-3180432.pdf

[50] *Mini-Circuits BLP-30+ Low-Pass Filter Datasheet*. p. 1. [Online]. Available: https://www.minicircuits.com/pdfs/BLP-30+.pdf

[51] *Mini-Circuits SHP-100+ High-Pass Filter Datasheet*. p. 1. [Online]. Available: https://www.minicircuits.com/pdfs/SHP-100.pdf

[52] *Mini-Circuits SLP-100+ Low-Pass Filter Datasheet*. p. 1. [Online]. Available: https://www.minicircuits.com/pdfs/SLP-100+.pdf

[53] *Mini-Circuits SHP-250+ High-Pass Filter Datasheet*. p. 1. [Online]. Available: https://www.minicircuits.com/pdfs/SHP-250+.pdf

[54] *Mini-Circuits SLP-300+ Low-Pass Filter Datasheet*. p. 1. [Online]. Available: https://www.minicircuits.com/pdfs/SLP-300+.pdf

[55] *Mini-Circuits SBP-70+ Band-Pass Filter datasheet*. p. 1. [Online]. Available: https://www.minicircuits.com/pdfs/SBP-70+.pdf

[56] *Mini-Circuits ZFDC-10-1-S+ Directional Coupler Datasheet*. p. 1. [Online]. Available: https://www.minicircuits.com/pdfs/ZFDC-10-1+.pdf

[57] *JFW 50-DR-060 Manual Attenuator DC-2000 MHz Datasheet*. p. 1. [Online]. Available: https://www.jfwindustries.com/pdf/50DR-060.pdf

[58] T. Kaisar, J. Lee, D. Li, S. W. Shaw, and P. X.-L. Feng, "Nonlinear stiffness and nonlinear damping in atomically thin MoS_2 nanomechanical resonators," *Nano Lett.*, vol. 22, no. 24, pp. 9831–9838, Dec. 2022.

[59] V. Kaajakari, T. Mattila, A. Oja, and H. Seppa, "Nonlinear limits for single-crystal silicon micro resonators," *J. Microelectromech. Syst.*, vol. 13, no. 5, pp. 715–724, Oct. 2004.

[60] R. Lifshitz and M. C. Cross, *Review of Nonlinear Dynamics and Complexity*. New York, NY, USA: Wiley, 2008.

[61] F. Reif, *Fundamentals of Statistical and Thermal Physics*. New York, NY, USA: McGraw-Hill, 1965.

[62] G. E. Uhlenbeck and L. S. Ornstein, "On the theory of the Brownian motion," *Phys. Rev.*, vol. 36, pp. 823–841, Sep. 1930.

[63] J. Lee, Z. Wang, K. He, J. Shan, and P. X.-L. Feng, "High frequency MoS_2 nanomechanical resonators," *ACS Nano*, vol. 7, no. 7, pp. 6086–6091, Jul. 2013.

[64] A. H. Nayfeh and D. T. Mook, *Nonlinear Oscillations*. New York, NY, USA: Wiley, 1979.

[65] H. W. C. Postma, I. Kozinsky, A. Husain, and M. L. Roukes, "Dynamic range of nanotube- and nanowire-based electromechanical systems," *Appl. Phys. Lett.*, vol. 86, no. 22, May 2005, Art. no. 223105.

[66] J. Lee and P. X.-L. Feng, "Self-sustaining MoS_2 nanomechanical oscillators and feedback cooling," *Appl. Phys. Lett.*, vol. 119, no. 24, Dec. 2021, Art. no. 243506.

[67] X. L. Feng, C. J. White, A. Hajimiri, and M. L. Roukes, "A self-sustaining ultrahigh-frequency nanoelectromechanical oscillator," *Nature Nanotechnol.*, vol. 3, no. 6, pp. 342–346, May 2008.

[68] D. B. Leeson, "Oscillator phase noise: A 50-year review," *IEEE Trans. Ultrason., Ferroelectr., Freq. Control*, vol. 63, no. 8, pp. 1208–1225, Aug. 2016.

[69] D. Ham and A. Hajimiri, "Virtual damping and Einstein relation in oscillators," *IEEE J. Solid-State Circuits*, vol. 38, no. 3, pp. 407–418, Mar. 2003.

[70] T. H. Lee and A. Hajimiri, "Oscillator phase noise: A tutorial," *IEEE J. Solid-State Circuits*, vol. 35, no. 3, pp. 326–335, Mar. 2000.

[71] A. Hajimiri and T. H. Lee, *The Design of Low Noise Oscillators*. Norwell, MA, USA: Kluwer, 1999.

[72] D. B. Leeson, "A simple model of feedback oscillator noise spectrum," *Proc. IEEE*, vol. 54, no. 2, pp. 329–330, Feb. 1966.

[73] A. Nikoofard, S. Kananian, and A. Fotowat-Ahmady, "Off-resonance oscillation, phase retention, and orthogonality modeling in quadrature oscillators," *IEEE Trans. Circuits Syst. I, Reg. Papers*, vol. 63, no. 6, pp. 883–894, Jun. 2016.

[74] M. Sansa et al., "Frequency fluctuations in silicon nanoresonators," *Nature Nanotechnol.*, vol. 11, no. 6, pp. 552–558, Jun. 2016.

[75] J. Rutman and F. L. Walls, "Characterization of frequency stability in precision frequency sources," *Proc. IEEE*, vol. 79, no. 7, pp. 952–960, Jul. 1991.

[76] D. W. Allan, "Time and frequency (time-domain) characterization, estimation, and prediction of precision clocks and oscillators," *IEEE Trans. Ultrason., Ferroelectr., Freq. Control*, vol. UFFC-34, no. 6, pp. 647–654, Nov. 1987.

[77] J. A. Barnes et al., "Characterization of frequency stability," *IEEE Trans. Instrum. Meas.*, vol. IM-20, no. 2, pp. 105–120, May 1971.

[78] K. L. Ekinci, Y. T. Yang, and M. L. Roukes, "Ultimate limits to inertial mass sensing based upon nanoelectromechanical systems," *J. Appl. Phys.*, vol. 95, no. 5, pp. 2682–2689, Mar. 2004.

[79] E. Mile et al., "In-plane nanoelectromechanical resonators based on silicon nanowire piezoresistive detection," *Nanotechnology*, vol. 21, no. 16, Mar. 2010, Art. no. 165504.

[80] T. L. Naing, T. O. Rocheleau, E. Alon, and C. T.-C. Nguyen, "A 78-microwatt GSM phase noise-compliant pierce oscillator referenced to a 61-MHz wine-glass disk resonator," in *Proc. Joint Eur. Freq. Time Forum Int. Freq. Control Symp. (EFTF/IFC)*, Jul. 2013, pp. 562–565.

[81] K. E. Wojciechowski, R. H. Olsson, M. R. Tuck, E. Roherty-Osmun, and T. A. Hill, "Single-chip precision oscillators based on multi-frequency, high-Q aluminum nitride MEMS resonators," in *Proc. Int. Solid-State Sensors, Actuators Microsyst. Conf.*, Jun. 2009, pp. 2126–2130.

[82] C. Zuo, N. Sinha, J. Van der Spiegel, and G. Piazza, "Multi-frequency pierce oscillators based on piezoelectric AlN contour-mode MEMS resonators," in *Proc. IEEE Int. Freq. Control Symp. (IFCS)*, Honolulu, HI, USA, May 2008, pp. 402–407.

[83] L. Comenencia Ortiz et al., "Low-power dual mode MEMS resonators with PPB stability over temperature," *J. Microelectromech. Syst.*, vol. 29, no. 2, pp. 190–201, Apr. 2020.

[84] Y. Yang, E. J. Ng, Y. Chen, I. B. Flader, and T. W. Kenny, "A unified *epi-seal* process for fabrication of high-stability microelectromechanical devices," *J. Microelectromech. Syst.*, vol. 25, no. 3, pp. 489–497, Jun. 2016.

[85] P. Ivaldi et al., "50 nm thick AlN film-based piezoelectric cantilevers for gravimetric detection," *J. Micromech. Microeng.*, vol. 21, no. 8, Jul. 2011, Art. no. 085023.

[86] M. Rinaldi, B. Duick, C. Zuniga, C. Zuo, and G. Piazza, "SS-DNA functionalized ultra-thin-film ALN contour-mode resonators with self-sustained oscillator for volatile organic chemical detection," in *Proc. IEEE 23rd Int. Conf. Micro Electro Mech. Syst. (MEMS)*, Jan. 2010, pp. 132–135.

[87] Y. Chen et al., "Ovenized dual-mode clock (ODMC) based on highly doped single crystal silicon resonators," in *Proc. IEEE 29th Int. Conf. Micro Electro Mech. Syst. (MEMS)*, Shanghai, China, Jan. 2016, pp. 91–94.

[88] A. Kourani, R. Lu, and S. Gong, "A wideband oscillator exploiting multiple resonances in lithium niobate MEMS resonator," *IEEE Trans. Ultrason., Ferroelectr., Freq. Control*, vol. 67, no. 9, pp. 1854–1866, Sep. 2020.

Tahmid Kaisar (Graduate Student Member, IEEE) received the B.S. degree in electrical and electronic engineering from the Bangladesh University of Engineering and Technology (BUET), Dhaka, Bangladesh, in 2018. He is currently pursuing the Ph.D. degree with the Department of Electrical and Computer Engineering (ECE), University of Florida, Gainesville, FL, USA.

His research interests include CMOS-MEMS oscillator-based computing, piezoelectric M/NEMS oscillators for real-time sensing and timing applications, nonlinear dynamics of M/NEMS resonators, and analog IC design.

Mr. Kaisar was a recipient of the Best Research Work Award at the AVS 2021 International Symposium.

S M Enamul Hoque Yousuf (Graduate Student Member, IEEE) received the B.S. degree in electrical and electronic engineering (EEE) from the Bangladesh University of Engineering and Technology, Dhaka, Bangladesh, in 2017. He is currently pursuing the Ph.D. degree with the Department of Electrical and Computer Engineering (ECE), University of Florida (UF), Gainesville, FL, USA.

His research interests include nano/microelectromechanical systems (N/MEMS), atomic layer semiconductors, phononic frequency comb, and transistors.

Mr. Yousuf was a recipient of the Margaret A. Ross Fellowship from ECE, UF (2020–2021). He was a recipient of the Best Student Presentation Award at the AVS 2021 International Symposium and one of the outstanding student paper award finalists at IEEE MEMS 2022 conference.

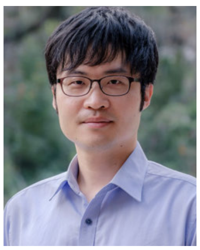

Jaesung Lee (Member, IEEE) received the B.S. and M.S. degrees in electrical engineering from The University of Electro-Communications (UEC), Tokyo, Japan, in 2007 and 2009, respectively, and the Ph.D. degree in electrical engineering from Case Western Reserve University (CWRU), Cleveland, OH, USA, in 2017.

He is currently an Assistant Professor with the Department of Electrical and Computer Engineering, University of Central Florida, Orlando, FL, USA. His research interests have focused on developing functional nanodevices (e.g., NEMS/MEMS, optoelectronic, and phononic devices) using advanced materials (e.g., 2-D crystals and wide bandgap semiconductors), toward building integrated systems for signal processing and sensing, in both classical and quantum regimes.

Dr. Lee is the Co-Technical Program Chair of the MEMS/NEMS Technical Group at the 69th American Vacuum Society (AVS) International Symposium and Exhibition.

Afzaal Qamar (Member, IEEE) received the M.Phil. degree in physics from the Pakistan Institute of Engineering and Applied Sciences (PIEAS), Islamabad, Pakistan, in 2006, and the Ph.D. degree from the Queensland Micro- and Nanotechnology Centre, Griffith University, Nathan, QLD, Australia, in 2017.

He worked as a Postdoctoral Research Fellow with the Department of Electrical Engineering and Computer Science (EECS), University of Michigan, Ann Arbor, MI, USA, from 2017 to 2020. His research interests are MEMS/NEMS devices, RF filters, piezoelectric and piezoresistive properties of wide bandgap (GaN, AlN, and SiC) semiconductors, and III–V-based photodetector.

Mina Rais-Zadeh (Senior Member, IEEE) received the B.S. degree in electrical engineering from the Sharif University of Technology, Tehran, Iran, in 2002, and the M.S. and Ph.D. degrees in electrical and computer engineering from the Georgia Institute of Technology, Atlanta, GA, USA, in 2005 and 2008, respectively.

From 2008 to 2009, she was a Postdoctoral Research Fellow with the Georgia Institute of Technology. In 2009, she joined the University of Michigan, Ann Arbor, MI, USA, as an Assistant Professor of electrical engineering and computer science (EECS), where she was a tenured Associate Professor in EECS from 2014 to 2018. She joined the NASA Jet Propulsion Laboratory (JPL), California Institute of Technology, Pasadena, CA, USA, in 2016, where she is currently leading the MEMS and micro-instrument development activity as a Group Supervisor for the Advanced Micro-Sensors and Micro-Systems Group.

Soumyajit Mandal (Senior Member, IEEE) received the B.Tech. degree from the Indian Institute of Technology (IIT) Kharagpur, Kharagpur, India, in 2002, and the S.M. and Ph.D. degrees in electrical engineering from the Massachusetts Institute of Technology (MIT), Cambridge, MA, USA, in 2004 and 2009, respectively.

He was a Research Scientist with Schlumberger-Doll Research, Cambridge, from 2010 to 2014; an Assistant Professor with the Department of Electrical Engineering and Computer Science, Case Western Reserve University, Cleveland, OH, USA, from 2014 to 2019; and an Associate Professor with the Department of Electrical and Computer Engineering, University of Florida, Gainesville, FL, USA, from 2019 to 2021. He is currently a Research Staff Member of the Instrumentation Division, Brookhaven National Laboratory, Upton, NY, USA. He has over 150 publications in peer-reviewed journals and conferences and holds 26 patents. His research interests include analog and biological computation, magnetic resonance sensors, low-power analog and RF circuits, and precision instrumentation for various biomedical and sensor interface applications.

Dr. Mandal was a recipient of the President of India Gold Medal in 2002, the MIT Microsystems Technology Laboratories (MTL) Doctoral Dissertation Award in 2009, the T. Keith Glennan Fellowship in 2016, and the IIT Kharagpur Young Alumni Achiever Award in 2018.

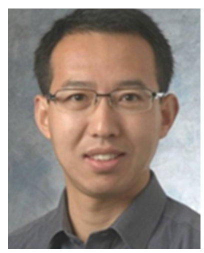

Philip X.-L. Feng (Senior Member, IEEE) received the Ph.D. degree in electrical engineering (EE) from the California Institute of Technology (Caltech), Pasadena, CA, USA, in 2007.

He is currently a Professor with the Department of Electrical and Computer Engineering, University of Florida, Gainesville, FL, USA. He has mentored/co-mentored 13 Ph.D. students to successful dissertation defense, mentored eight postdoctoral scholars, and also supervised 15 M.S. students with theses or research projects. His research is primarily focused on emerging solid-state devices and systems, particularly nano/microelectromechanical systems (NEMS/MEMS), atomic layer semiconductors and 2-D heterostructure devices, silicon carbide (SiC) and other wide/ultrawide-bandgap (WBG/UWBG) semiconductors, quantum devices based on SiC and 2-D materials, as well as their integration with state-of-the-art ICs and optical/photonic technologies.

Dr. Feng was an invited participant to the National Academy of Engineering (NAE) U.S. Frontiers of Engineering (USFOE) Symposium in 2013 and subsequently a recipient of the NAE Grainger Foundation Frontiers of Engineering (FOE) Award in 2014. His awards also include the National Science Foundation CAREER Award in 2015 and the Presidential Early Career Award for Scientists and Engineers (PECASE) in 2019. He and his students have won six best paper/presentation awards from IEEE and other international conferences. He has served on the Technical Program Committees (TPCs) for the IEEE International Electron Devices Meeting (IEDM), the IEEE International Conference on Micro Electromechanical Systems (MEMS), the International Conference on Solid-State Sensors, Actuators and Microsystems (Transducers), the International Frequency Control Symposium (IFCS), IEEE Sensors, and other international conferences. He served as the Track Chair for IEEE Sensors from 2016 to 2017 and the TPC Group IV Chair for the IEEE IFCS from 2018 to 2020. He has also served as the Technical Program Chair for the MEMS/NEMS Technical Group from the 61st to 63rd American Vacuum Society (AVS) International Symposium and Exhibition. Since 2017, he has been a Co-Organizer and the Technical Chair of the SiC Materials and Devices Workshop. He has served as the Chair for the 34th IEEE International Conference on Micro Electromechanical Systems (IEEE MEMS 2021). He has also co-organized and co-chaired the Florida Semiconductor Week (FSW) Workshop in January 2023.